Physics – Uspekhi **69** (3) 246 – 269 (2026)

CONFERENCES AND SYMPOSIA

PACS numbers: 95.55.Jz, 98.58.Ec, **98.62. – g**

Multi-frequency radio monitoring on RT-22 in Simeiz: variability, structure and gravitational-wave prospects of binary supermassive black holes and galactic kilomasers *

A.E. Volvach, L.N. Volvach, M.G. Larionov

DOI: https://doi.org/10.3367/UFNe.2025.03.039932

Contents

Abstract. Using the 22-meter RT-22 radio telescope (Simeiz), a unique database on the variability of active galactic nuclei (AGN) in the centimeter and millimeter wavelength ranges has been created. This database is virtually the only one of its kind in the world in this frequency range. A special class of AGNs has been identified — tight binary systems of supermassive black holes (SMBHs) at an evolutionary stage close to merger, exhibiting quasi-periodic variability in their emission. Statistical analysis indicates that, due to beaming effects, only about 1% of such systems are observable. We present results of long-term, multi-frequency radio monitoring of several AGNs suspected of harboring binary SMBHs: 3C 273, 3C 454.3, S5 0528 + 134, and AO 0235 + 164. Based on these observations, a new model is proposed for estimating the parameters of tight binary SMBHs solely from radio data. An energy balance analysis demonstrates that standard accretion onto a single SMBH cannot account for the observed emission power. An alternative model is proposed, in which the primary energy release is caused by the secondary SMBH traversing a common accretion environment. The methodology for determining the physical parameters of the SMBHs includes harmonic and wavelet analyses, as well as estimation of companion masses and orbital parameters. The results suggest that these systems may consist of extremely massive and compact binaries with nearly equal-mass components. The most massive binary black hole (3C 454.3) and the most powerful radio emitter in the Universe (S5 0528 + 134, 'Nimfa') have been identified. For the first time in global practice, the phenomenon of giant flares of water maser emission in Galactic sources has been discovered using the RT-22 radio telescope of the Crimean Astrophysical Observatory. We present the results of long-term monitoring of water kilomasers in the Galactic sources IRAS 18316 – 0602 and W51 Main at the 22.35 GHz line. It has been established that IRAS 18316 – 0602 is the most powerful water kilomaser in the Galaxy. This discovery was included in the annual report of the Russian Academy of Sciences to the President of the Russian Federation as one of the most significant astrophysical achievements of 2019. Such results have been obtained for the first time in the global scientific community. A methodology has been developed to estimate the level of gravitational radiation from tight binary SMBHs and compact binary stellar systems. The flux of gravitational waves reaching the Earth from such sources has been estimated, showing that it is potentially detectable by gravitational wave detectors such as the International Pulsar Timing Array (IPTA). This opens up new broad possibilities for further research of gravitational waves with the aim of their experimental detection.

Keywords: active galactic nuclei; binary supermassive black holes; star-forming regions; masers; gravitational waves

A.E. Volvach [1, *], **L.N. Volvach** [1], **M.G. Larionov** [2]

[1] Crimean Astrophysical Observatory, Russian Academy of Sciences, pos. Nauchny, Bakhchisaraiskii region, 298409 Crimea, Russian Federation

[2] Lebedev Physical Institute, Russian Academy of Sciences, Leninskii prosp. 53, 119991 Moscow, Russian Federation

E-mail: [*] volvach@bk.ru

Received 10 May 2025

Uspekhi Fizicheskikh Nauk **196** (3) 264 – 289 (2026)

Translated by V.L. Derbov

* This review is based on the report presented for the Scientific Session of the Physical Sciences Division of the Russian Academy of Sciences (PSD RAS), on March 19, 2025 (see *Physics–Uspekhi* **69** (3) 221 (2026); *Uspekhi Fizicheskikh Nauk* **196** (3) 238 (2025)).

1. Introduction: The RT-22 radio telescope in Simeiz — from concept to epoch-making discoveries

The development of radio astronomy in the second half of the 20th century was a crucial stage in the formation of modern astrophysics. Along with classical optical observation tools, radio telescopes opened a fundamentally new range — millimeter, centimeter, and meter wavelengths — making it possible to peer into the depths of the Galaxy and distant regions of the Metagalaxy.

In this context, the construction and development of the RT-22 radio telescope at the Crimean Astrophysical Observatory in Simeiz became key events in the history of Russian science. The work began in November 1959 as part of a strategic program for the development of radio astronomy. The project envisioned the creation of a high-precision parabolic mirror 22 meters in diameter, designed to receive radio waves in the centimeter and millimeter ranges. Construction and installation work was completed by 1965, and the first experimental observations began in September 1966 (Photo 1).

Thanks to its favorable geographic location — an open horizon and natural protection from radio interference from the northern side by the Crimean Mountains — as well as its well-thought-out design, the RT-22 quickly became one of the most sensitive observing facilities of its class in the USSR and received international recognition.

Amid growing interest in high-frequency radio astronomy in the 1960s, the task was set to conduct the first Soviet sky survey in the short-wavelength centimeter range (3 cm wavelength). The goal was to identify new radio sources with spectral peaks in the high-frequency range and objects with pronounced variability. This led to the Simeiz Sky Survey 'S' — one of the first in the world in this range. To implement it, the RT-22 receiving system was upgraded, and an original data acquisition and processing system was developed, including magnetic recording and automated computer-assisted interpretation.

During pilot observations in 1969, a preliminary catalog of sources was compiled. One of the most important discoveries was the object S0528 + 134 (Nimfa), the first blazar discovered in the USSR. It turned out to be an active nucleus with high variability, a compact structure, and a maximum emission in the centimeter range. It was later established that Nimfa is one of the most powerful sources of barometric luminosity in the Universe: according to modern estimates, the mass of its central black hole reaches $\approx 3.6 \times 10^{10}\, M_{\odot}$, and the radiated power is $\sim 10^{48}$ erg s^{-1}.

In parallel, very-long-baseline interferometry (VLBI) was developed, making it possible to overcome the angular resolution limitations of single telescopes. This work required the creation of highly accurate time and frequency standards, which stimulated the development of hydrogen frequency standards.

In 1973, the RT-22 participated in the world's first intercontinental VLBI experiment, achieving a record-breaking angular resolution at the time. This event became a major milestone in global radio astronomy and laid the foundation for future geodynamic and space programs, including the RadioAstron mission.

Thus, from the moment of its origin, the RT-22 not only became the first instrument in the USSR to peer into the millimeter range, but also served as a technological and scientific platform that ushered in a new era of radio astronomy — the era of high-precision interferometry and the search for compact variable sources. This radio telescope was more than just an observational instrument; it was a true experimental laboratory where new methods, concepts, and approaches were developed, many of which later became global standards.

Photo 1. First experimental observations, 1966.

Research into active galactic nuclei (AGN) became one of priorities. Multifrequency monitoring using RT-22 allowed studying spectral and temporal variability, identifying quasi-periodic components and activity bursts associated with the dynamics of the accretion disk and jets. This resulted in the creation of a unique database, one of the largest in the world, actively used to interpret energy release processes, test accretion models, and coordinate international observation campaigns.

RT-22 also made a significant contribution to the study of galactic kilomasers — sources of coherent radio emission in the H_2O, OH, CH_3OH, and CO lines. Thanks to its high sensitivity and spectral resolution (up to 0.02 km s^{-1}), masers were studied in star-forming zones, the envelopes of late stars, and comet atmospheres. Two kilomasers were detected, including the most powerful in the Galaxy. In some cases, observations were conducted as part of VLBI networks, which made it possible to obtain maser spot maps with an angular resolution of up to milliseconds of arc and study the kinematics of the sources.

The participation of RT-22 in the radio astronomy diagnostic complex of the Solar Service KRIM (which also includes RT-2, RT-3, and RT-M) plays an important applied role. The complex provides multi-band monitoring of solar activity and is part of an international observing network. A method for short-term solar flare forecasting based on spectral-probability analysis of radio and X-ray radiation received from both ground-based and space-based observatories has been developed and patented.

From the very beginning, the RT-22 has been used in a number of applied fields. As part of the Vega mission (1984–1986), it provided telemetry reception from balloon probes in the atmosphere of Venus. Despite a distance of over 100 million km and a signal power of only 1 watt, it was possible to achieve an accuracy of up to 200 m in determining the probes' positions, at a velocity of approximately 50 m s^{-1}.

A VLBI location method — a combination of radar and VLBI — was developed and tested using the RT-22 and other antennas in the VLBI network. It was used to

Photo 2. The 22-meter RT-22 radio telescope in Simeiz, 2023.

measure the motion parameters of planets, asteroids, and space debris. The method has proven effective both in fundamental astrometry and in ensuring the safety of space activities.

In the 1990s, the RT-22 became the instrument for the first VLBI experiments on geodynamics in the CIS. As part of the Geodynamics project, the absolute and relative velocities of Crimea's movement were determined with millimeter accuracy, its tectonic activity was identified, and a model of the region's deformations was constructed. Based on this data, the Simeiz–Katsiveli scientific testing ground was established, where methods for detecting earthquake precursors are being further developed. These include a patented method for analyzing the entropy of the geomagnetic field and approaches based on the parametric resonance of geomagnetic surface waves.

Experience accumulated in geodynamic projects formed the basis for the creation of the domestic KVAZAR-KVO VLBI network, which formed the basis of the Russian Federation's coordinate-time support system and the development of the domestic implementation of the International Celestial Coordinate System.

Thus, the history of the RT-22 is a journey from an engineering idea to a highly complex scientific instrument that has influenced a wide range of areas of modern science, from cosmology to geophysics. Today, the RT-22 radio telescope remains one of the best radio telescopes in Russia and is among the top five radio telescopes in the world operating in the millimeter wavelength range (Photo 2).

This review focuses on the results of long-term monitoring of active galactic nuclei and the discovery of galactic kilomasers, accomplished using the RT-22 radio telescope in Simeiz.

2. Determining the parameters of binary supermassive black holes from multi-frequency radio monitoring data: examples of the blazars 3C273, 3C 454.3, S0528 + 134, and AO 0235 + 164

2.1 Introduction

It has been suggested that some of the brightest active galactic nuclei (AGN) are compact formations in the central regions of massive elliptical galaxies containing close binary systems of supermassive black holes (SMBHs) elliptically orbiting a common center of mass [1]. Such systems may be in the final stages of evolution, close to merger. They constitute only a small fraction of the total number of AGNs and represent a special class of objects exhibiting quasi-periodic variations in their emission. The presence of a close binary SMBH may be a key factor in the enormous energy release observed in such objects.

Statistical studies show that the density of radio sources with fluxes above 1 Jansky (Jy) at 20 GHz is approximately 25 sources per steradian. Of these, approximately 50% exhibit flat or inverted spectra, making it possible to estimate the total number of bright AGNs on the celestial sphere at ~ 150. The proportion of sources with flat spectra decreases with decreasing flux: at the 0.1 Jy level, it is only $\sim 25\%$. This indicates that fainter sources are less represented among such AGNs.

Observations show that bright AGNs can form as early as redshifts of $z \geqslant 2$, as in the case of S0528 + 134. This means that SMBHs with masses of $M \geqslant 10^9\, M_\odot$ already existed at relatively early stages of the Universe evolution. Moreover, such systems are capable of emitting radiation fluxes of about ≈ 10 Jy, and it is possible that up to $z \approx 5-6$ Jy they can be observed. However, the mass number of such objects at high z has not been recorded, which indicates a peak in their formation at $z \approx 2-3$.

To estimate the true number of such sources, it is necessary to consider their emission geometry: relativistic jets from AGNs are directed in a narrow cone about $5-6^\circ$. Consequently, only $\sim 1\%$ of their total number can be observed, yielding an estimate of $\sim 1.5 \times 10^4$ potential AGNs with binary SMBHs. This is approximately 10^{-6} of the number of all massive galaxies in the Universe ($\sim 10^{10}$), resulting in a short active phase of the order of 10^4 years.

Of these 15,000 objects, only about 150 are observed to be bright representatives of active galactic nuclei with narrow-beam emission. Their characteristic feature is the presence of pronounced quasi-periodicity in luminosity variations, reflecting the dynamics of the binary system.

A significant question is the source of the colossal energy of these systems [2, 3]. Using several AGNs as examples, we have provided explanations for the presence of the variability phenomenon in such AGNs [3–5]. Another type of explanation for the binarity of supermassive black holes was given by Yi-Fan Wang and Yun-Guo Jiang, who explained the flux density variation only by a change in the inclination angle between the emissions from the source and the direction toward the observer, although internal causes such as the inverse Compton effect were not excluded [6].

This paper presents the results of long-term multi-frequency radio monitoring of the blazars 3C 273, 3C 454.3, S 0528 + 134, and AO 0235 + 164, carried out with the RT-22

radio telescope in Simeiz. A model is proposed that makes it possible to determine the parameters of close binary SMBHs based solely on radio observations: component masses, orbital sizes, velocities, system kinetic energy, energy loss to gravitational radiation, and the lifetime of the objects before merger. Attention is also paid to the prospects of detecting the gravity-wave signal from such systems using instruments including the International Pulsar Timing Array (IPTA), the NANOGrav, and the EPTA. The model is also considered using massive binary stars as an example.

2.2 Observation and data processing methodology

Data of observations at frequencies of 4.8, 8, 14.5, 22.2, and 36.8 GHz were obtained using the 22-meter RT-22 radio telescope of the Crimean Astrophysical Observatory. For monitoring at a frequency of 14.5 GHz, the 26-meter radio telescope RT-26 of the University of Michigan Observatory was used from 1974 to 2012. Data on this source were previously published and used in [4–6]. Observations at a frequency of 15 GHz were carried out using the 40-meter radio observatory Ovens Valley from 2013 to 2019 [7]. Multi-frequency long-term monitoring of the objects AO 0235 + 164, 3C 454.3, S 0528 + 134, and 3C 273 is presented in Figs 1a–d

The receiving system utilized a beam-modulated radiometer, which minimized distortions caused by anomalous fluctuation spectra in the amplifier gains, as well as temperature fluctuations due to atmospheric inhomogeneities, which are particularly noticeable at centimeter and millimeter wavelengths. The signal was recorded as the difference in antenna temperatures at various radio telescope positions (on the source and off it, using the 'on–on' reception method). In each measurement, the radio telescope was alternately set on one receiving horn and then on the other. Each observation consisted of 5–20 individual measurements, followed by calculation of the mean value and the standard error of mean. Temperature calibration of the measurements was performed using the 'atmospheric cutoff' method at intervals of 3–4 hours. Antenna temperatures were recorded at various radio telescope elevation angles. Objects with pre-known characteristics, the parameters of which are given in Table 1, were used as calibration sources.

Harmonic analysis.

To assess the reliability of events and the probability of false alarms, our studies employed one of the most commonly used practical power spectrum estimators — the least-squares spectral analysis (LSSA) [8–10]. Its mathematical apparatus was developed in Refs [11–13]. The LSSA spectrum is constructed by approximating a time series by a sum of harmonic functions using the least-squares method. One of the advantages of the LSSA is its ability to account for the exponential distribution of white noise periodogram readings. However, its main drawback is the lack of a direct analytical relation between the power spectrum estimate and its true value.

To address this drawback, Schuster's method [5], which is more suitable for spectral analysis, was used. The calculation of the Schuster periodogram $D(\omega)$ associated with the true power spectrum and the spectral window $W(\omega)$ is carried out according to the fundamental relation [14, 15]:

$$D(w) = \int_{-\infty}^{+\infty} g(w')\,W(w - w')\,\mathrm{d}w'. \qquad (1)$$

Table 1. Flux densities for calibration sources at frequencies of 4.8–36.8 GHz.

4.8 GHz	Source	3C 144	3C 274	M 17	3C 405
	Flux density, Jy	612.9	71.4	584.8	378.2
8 GHz	Source	DR 21	3C 274	3C 144	3C 353
	Flux density, Jy	21.6	49.1	585.0	15.5
14.5 GHz	Source	3C 144	3C 274	DR 21	3C 405
	Flux density, Jy	446.2	29.1	20.2	94.3
22.2 GHz	Source	DR 21	3C 274	NGC 7027	3C 286
	Flux density, Jy	19.5	21.5	5.9	2.4
36.8 GHz	Source	DR 21	3C 274	NGC 7027	3C 286
	Flux density, Jy	18.3	14.3	5.1	1.56

This ratio allows for 'cleaning' the spectrum by removing unnecessary peaks associated with a finite and unevenly distributed time grid, as well as false peaks arising from noise. To 'clean' the spectrum, we used the CLEAN method, which was originally developed for processing two-dimensional maps obtained during aperture synthesis and later adapted for spectral analysis of one-dimensional time series [17]. The CLEAN method consists of sequentially subtracting all significant maxima from the 'dirty' spectrum. Each subtracted spectral peak is defined by its complex amplitude, frequency, and spectral window, which depends on the time distribution of the data. The 'cleaning' process continues until no peaks remain in the spectrum whose value exceeds a threshold level determined by the probability of detecting a signal in noise. This threshold can be calculated knowing the distribution type of the noise periodogram samples [13, 17]. For a nonuniform time grid, a rigorous analytical expression for the noise distribution is lacking. Empirical formulas exist for such series, although their generality is limited and they can be specific to each particular series [17].

The process of removing false peaks allows us to obtain a clean spectrum free of noise and false maxima. As a result of applying the CLEAN method, variations in the light curves with different periods were revealed for each source. For the blazar AO 0235 + 164, these data are presented in Table 2. All values given in Table 2 correspond to peaks in the power spectrum exceeding the 5σ level.

Figure 2 shows the results of the harmonic analysis for AO 0235 + 164 in the radio range at a frequency of 8 GHz. The red line represents the level of five standard deviation for the spectral signal density. The abscissa shows the harmonic frequencies expressed in units of $1/T$, where T is the period in years.

One of significant results is a period of 3.8 years, although its physical explanation remains unclear. Other studies mention a period of approximately 8 years. Roy et al., for example, analyzed optical data (in the R-band) of the blazar AO 0235 + 164 for the period from 1982 to 2019 and found a flux density periodicity of 8.13 years [18]. This period is also present in our studies, but its amplitude is approximately one and a half times smaller than that of the other period, the 6 year one, we also discovered. Although both periods are observed, we preferred the 6 year period due to its higher significance level.

Correlation Analysis.

The Crimean Astrophysical Observatory (CrAO) database contains observation records of various astronomical

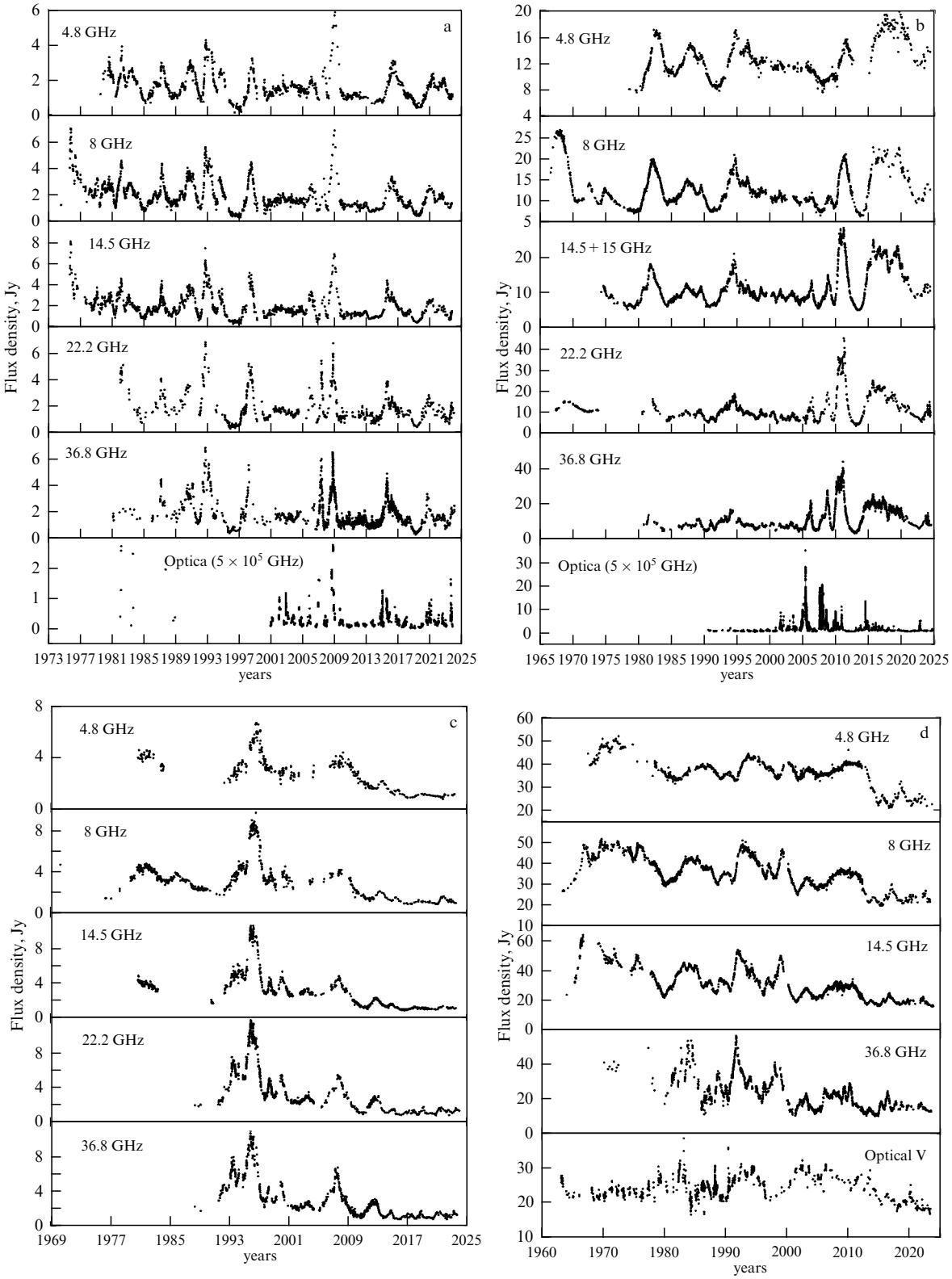

Figure 1. Multi-frequency monitoring of the blazars AO 0235 + 164 (a), 3C 454.3 (b), S 0528 + 134 (c), and 3C 273 (d) in the radio range.

sources at several frequencies in obtaining which we actively participated. Determining the phase relationships between oscillations at different observation frequencies allows extracting information about the properties of the medium in which these oscillations propagate. To reveal the time shift between two records, it is necessary to calculate their mutual correlation function $R(\tau)$:

$$R(\tau) = \lim_{T\to\infty} \frac{1}{T} \int_0^T x_1(t) X_2(t+\tau)\, \mathrm{d}t\,. \qquad (2)$$

Since the signals under study are recorded at specific, generally nonequidistant points in time t_i, we have to deal

Table 2. Harmonic analysis data for flux variations of AO 0235 + 164 at different frequencies.

Frequency	Period (years)	FAP[1]	Period (years)	FAP[1]	Period (years)	FAP[1]
8.0 GHz	5.6 ± 0.4	0.0002	1.8 ± 0.3	0.0008	1.0 ± 0.1	0.001
14.5 GHz	5.7 ± 0.4	0.0001	1.9 ± 0.3	0.0003	1.0 ± 0.1	0.001
36.8 GHz	6.0 ± 0.3	0.0003	2.0 ± 0.3	0.0005	1.2 ± 0.2	0.001
Average over all frequencies	6.0 ± 0.2		2.0 ± 0.1		1.0 ± 0.05	
Period in the reference frame associated with the source	75 ± 2.5		25 ± 1.5		12 ± 0.7	

[1] False alarm probability (FAP).

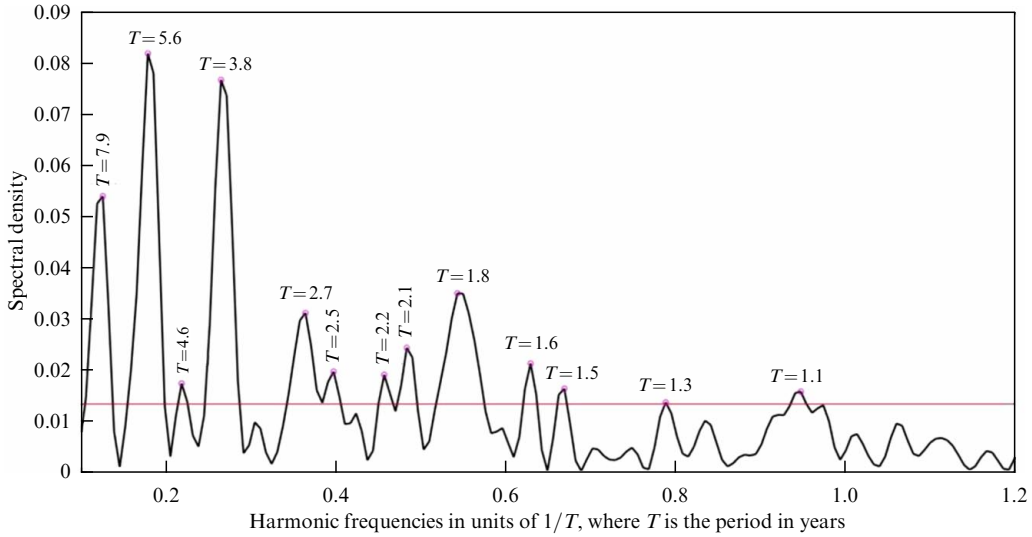

Figure 2. Results of harmonic analysis for AO 0235 + 164 in the radio band at a frequency of 8 GHz.

with discrete time functions or time series x_i. Furthermore, the observations last for a finite time, so the series under consideration are limited. In this case, it is impossible to determine the correlation function using Eqn (2). Therefore, an estimate of the correlation function, called the correlogram C_m, is often used [15].

$$C_m = \frac{1}{N-m} \sum_{k=0}^{N-m-1} (x_k - \bar{x})(y_{k+m} - \bar{y})$$
$$m = 0.1, \ldots, N-1\,. \qquad (3)$$

It should be noted that the coefficient $1/(N-m)$ in Eqn (3) is introduced to eliminate correlogram distortion associated with the finiteness of the time series; therefore, this estimate is called biased. To normalize the estimate C_m, it is divided by the product of the standard deviations of the series $\sigma_x \sigma_y$, where

$$\sigma_x^2 = \frac{1}{N-1} \sum_{k=0}^{N-1} (x_k - \bar{x})^2\,, \qquad (4)$$

$$\sigma_y^2 = \frac{1}{N-1} \sum_{k=0}^{N-1} (y_k - \bar{y})^2\,, \qquad (5)$$

The above applies to the simplest case of a uniform distribution of time samples. However, the time series we use have an uneven time grid. Therefore, the use of classical methods for finding estimates of cross-correlation functions is impossible.

One way to solve this problem is to interpolate the nonuniform series onto a uniform time axis. Equation (2) is then used to calculate the estimate of the correlation function. In this case, each sample, regardless of whether it was actually recorded or is the product of interpolation, makes an equal contribution to the desired correlation function. Furthermore, a significant drawback of this method is the impossibility of determining the theoretical reliability of the result obtained.

Another approach to determining estimates of the cross-correlation functions of nonuniform time series, free from these drawbacks, is substantiated in detail in Ref. [19]. In their study, the authors propose to use the so-called discrete correlation function (DCF), defined using the set of all possible correlations UDCF_{ij} (Unbinned Discrete Correlation Function), as follows:

$$\mathrm{UDCF}_{ij} = \frac{(x_i - \bar{x})(y_j - \bar{y})}{\sqrt{(\sigma_x^2 - e_x^2)(\sigma_y^2 - e_y^2)}}\,. \qquad (6)$$

Here, e_x, and e_y are the measurement errors of the random variables x and y, respectively. Each value of the UDCF_{ij} has its own delay. To calculate the maximally discrete correlation function $\mathrm{DCF}(\tau)$, the time axis is divided into a certain number of intervals $\Delta\tau$ (bins), after which each interval is assigned the average value of all UDCF_{ij} for which

$\tau - \Delta\tau/2 \leqslant \Delta\tau_{ij} < \tau + \Delta\tau/2$:

$$\mathrm{DCF}(\tau) = \frac{1}{M}\sum \mathrm{UDCF}_{ij}\,. \tag{7}$$

When choosing the bin size, one should be guided by the set goals, since the wider the bin, the better the averaging equation (6), but at the same time, the worse the temporal resolution of the x-axis, and vice versa.

Often, when simultaneous observations are made in time series, intense correlated spurious peak measurement errors arise at $\tau = 0$. When choosing the bin size, one should be guided by specific goals, since the wider the bin, the better the averaging equation (4), but the worse the temporal resolution of the x-axis, and vice versa.

This method allows one to easily obtain the standard deviation of the obtained values of $\mathrm{DCF}(\tau)$. If the UDCF_{ij} values are uncorrelated within a given bin, the standard deviation is determined by the dispersion of the UDCF_{ij} values around the mean $\mathrm{DCF}(\tau)$. To eliminate the influence of these errors, it is necessary to exclude from the set of UDCF_{ij} all elements for which $i = j$. In this case, all remaining correlogram readings are free of these errors, which is not the case when using the interpolation method.

$$\sigma^2_{\mathrm{DCF}}(\tau) = \frac{1}{N-1}\sum \left(\mathrm{UDCF}_{ij} - \mathrm{DCF}(\tau)\right)^2. \tag{8}$$

Thus, the method for constructing estimates of cross-correlation functions described in Ref. [19] has a number of significant advantages over the interpolation method. An undeniable advantage is the ability to determine the reliability of the obtained result. In our study, both approaches were used for comparison. An example of cross-correlation of observational data in the optical and radio ranges (36.8 GHz) for AO 0234 + 164 is shown in Fig. 3.

Correlations and delays are inherently significant, since they occur with significant harmonics. We obtained an empirical dependence of flare delays at different frequencies, which can be approximated by an inverse logarithmic dependence:

$$\Delta T = k\,\frac{0.25}{\log \nu}\,, \tag{9}$$

where ΔT is the delay, expressed in years from the flare onset in the optical range (V-band) and 36.8 GHz, ν is the observation frequency in GHz, and k is a coefficient. This dependence was derived empirically. For flare events, time shifts were determined using the described cross-correlation method. This pattern of delay variation with frequency rather suggests internal factors causing flux density variations in AGN. The dependence of event delays on frequency in the case of intergalactic scintillations differs from the frequency dependence [20].

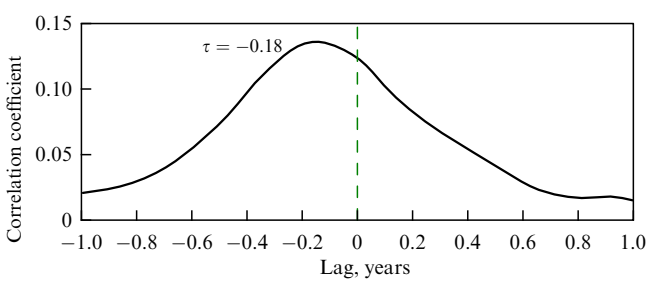

Figure 3. Cross-correlation of observational data between the optical (V) and radio (36.8 GHz) bands for AGN AO 0235 + 164. The abscissa shows frequencies of harmonic in units of $1/T$, where T is the period expressed in years.

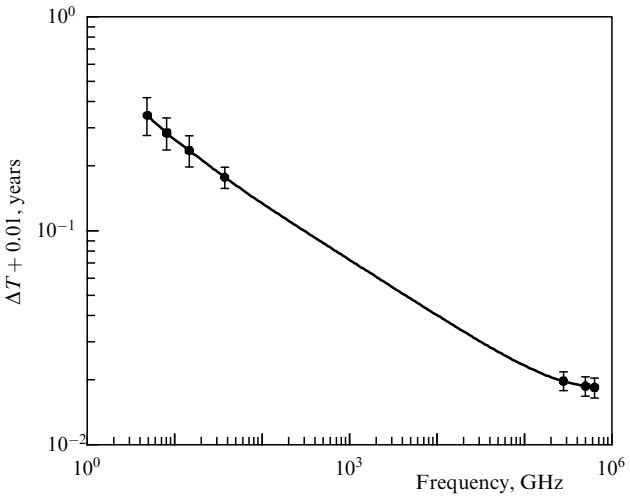

Figure 4. Dependence of flare onset delays at frequencies of 4.8 GHz, 8 GHz, 14.5 GHz, 36.8 GHz, 2.8×10^5 GHz (J), 5×10^5 GHz (R) relative to the optical (V) 6.36×10^5 GHz for 3C 454.3.

For the 2015 flare (see Fig. 1), the cross-correlation method was used to determine the delays between the optical wavelength range (V) and millimeter waves (36.8 GHz and 22.2 GHz). They were found to be 21 and 8.2 days, respectively. This allowed us to determine the coefficient in Eqn (9). The resulting value of the coefficient k is ≈ 1.5. The dependence of the flare onset delays at frequencies of 22.2 GHz and 36.8 GHz with respect to the optical wavelength range (V) for 3C 454.3 is shown in Fig. 4.

After 2009, the flare activity of the source S0 528 + 134 (Fig. 1b) began to fade. A consequence of this may be a change in the angle between the jet from the source and the direction at the observer. This was reflected in the fact that the delays between frequencies decreased by a factor of 2.5 compared to the flare of 2008–2009. In Ref. [5], based on the analysis of observational data, it was suggested that the magnitude of the delays of flare events at different frequencies is a quadratic function of the angles between the direction of the emissions and the line of sight of the observer. According to observational data, these angles in AO 0235 + 164 should be in the range of (2°–3°). According to Refs [21, 22], this angle is 2.9°, which corresponds to a Lorentz factor of $\gamma = 20$. For small values of θ, there is a relation linking this angle with the Lorentz factor, as mentioned above, $\gamma = 1/\theta$. Lorentz factors of 30–40 were obtained based on the VLBI data for components propagating along the jet [23]. This means that the source activity may vary with time depending on its internal properties and the orientation of the emissions depending on their direction toward the observer.

Wavelet analysis.

To reveal possible changes in the values of the periodic components throughout the entire monitoring period, wavelet analysis of the data was used. It consisted of the following steps. A 12-year observation cycle (half the original monitoring time) was studied using harmonic analysis. The 12-year duration was chosen so that the 6-year precession period fit twice. Next, a sliding shift of the 12-year data set was

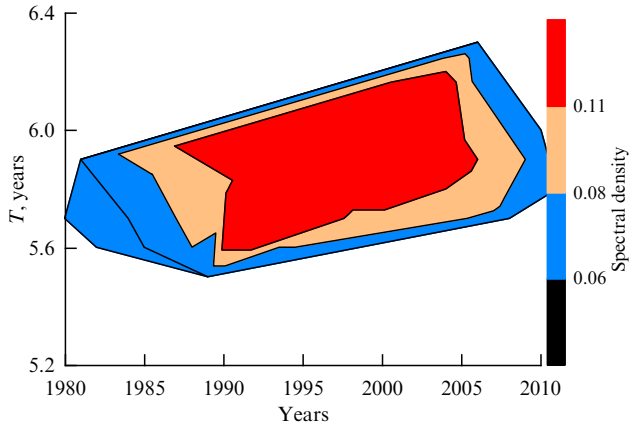

Figure 5. Wavelet analysis data for the blazar AO 0235 + 164. The period in years (left ordinate) versus time (abscissa) is plotted for the period 1980–2010. The spectral flux density is on the right ordinate.

performed at 1-year intervals toward increasing the observation period. In each case, a harmonic analysis of the 12-year data was performed. The results are presented in Fig. 5, where the period change is plotted versus time for AO 0235 + 164 for the time interval 1980–2010. The change in the 6-year period over 25 years was 0.2 years, which is less than the error in determining this period. Thus, no changes in the periods were detected within the error limits.

2.3 Determining the parameters of the binary supermassive black hole

Table 2 presents the results of the harmonic analysis of the flux variations for AO 0235 + 164 at different frequencies. A period of 6 years is reliably identified. This period may be associated with the presence of precessional motions of the central SMBH and accretion disk (AD), associated with it. Shorter periods of 2.0 and 1.0 years are distinguished at all radio frequencies. They can be associated with the period of the companion's orbital motion. The period of 1.0 years is explained by the companion crossing the AD twice during a 2-year orbital period. Other intermediate periods may be associated with the periods of nutation or combination periods in the system, which, in addition to the central body, also has an AD and a mass of accreting matter.

The period of 6 years may be precessional, as is the case with other bright AGN [24]. The spread of values for this period does not exceed the limits of statistical error. Harmonic components of flux density variations, inferred from the SMBH, have been used in a number of studies. Thus, for 3C 120, the values $T_{\rm pr} = 12.3$ years and $T_{\rm orb} = 1.4$ years are given [25, 26]. In source OJ287, two periods are distinguished (one is 11.65 years, the second is 1.1 or 1.6 years) based on optical data [27–29]. For 3C 273, precessional and orbital periods of 12.4 and 3.0 years are distinguished [3].

The amplitudes of the periods of 6.0, 1, and 2 years (75, 12, and 25 years in the initial coordinate system) have maximum values compared to other periods. There is a set of intermediate combination periods from 3 years to 5.5 years, with smaller amplitudes, which, as was said, can be explained by variations in the motions of a system consisting of more than two bodies, to which a massive AD and an accreting medium are added [30].

The dataset obtained in the optical range is more limited compared to the radio range (R-band, lower panel, Fig. 1). However, their analysis yields the same orbital and precessional periods as in the radio range. This confirms our assumptions that using only radio-frequency data allows us to obtain the main results in determining the characteristics of the SMBHs studied.

Roy analyzed optical (R-band) data for the blazar AO 0235 + 164 for the period 1982–2019. As a result, a periodicity of flux density variations of ~ 8.13 years was discovered [31]. The difference in the two-year periods obtained by Roy and us is possibly due to the shorter data sample that we used in our analysis. Expressions for the SMBH parameters, obtained based only on radio monitoring, allow us to estimate the following physical characteristics: companion masses and orbital sizes. The relations for calculating the numerical data are obtained based on Kepler's laws and lead to the following results [4]:

$$m = \frac{16\pi^2 R^3}{3GT_{\rm orb}T_{\rm pr}}, \quad M = \frac{16\pi^2 R^3 (0.75T_{\rm pr} - T_{\rm orb})}{3GT_{\rm orb}^2 T_{\rm pr}}. \qquad (10)$$

Here m and M are the mass of the satellite, R is the radius of the satellite's orbit, and $T_{\rm pr}$ and $T_{\rm orb}$ are the precession periods of the central body and the orbital period of the satellite, respectively.

The data for $T_{\rm pr}$ and $T_{\rm orb}$ obtained from the radio data (Table 2, last row) can be substituted into Eqn (10). Further, to find the period results in the coordinate system associated with the observations, it is necessary to take into account the influence of the relativistic γ-factor.

$$T_{\rm source} \approx \frac{T_{\rm observ}\gamma^2}{1+z}. \qquad (11)$$

This leads to the following period values in the source-related coordinate system: $T_{\rm source,\,pr} \approx 75$ years and $T_{\rm source,\,orb} \approx 25$ years. AO 0235 + 164 is a unique system from the point of view of the closeness of its companion masses. According to the expression (10) for the mass ratio: $(M+m)/m \approx 0.75(T_{\rm pr}/T_{\rm orb})$, $M \approx 1.25m$.

Analyzing expression (10), we can see that there is a cubic relationship between the satellite masses and their orbital radii. This allows establishing the possible range of satellite orbital sizes using certain additional physical conditions. These conditions include a limit on the mass of binary SMBHs, which cannot exceed tens of billions of solar masses; otherwise, the stability of the gravitational field may be compromised. The lower mass limits are associated with the large observed radiation powers from objects over a wide range of wavelengths and the extremely short lifetime of the source due to energy loss during gravitational radiation [13]. These constraints allow us to estimate the range of satellite masses and their orbital values with permissible errors based on Eqn (10): $m \approx 6.0 \times 10^9\, M_\odot$, $M \approx 7.5 \times 10^9\, M_\odot$, $R_{\rm comp} \approx 2 \times 10^{17}$ cm. Using a precession period of 8 years (100 years in the coordinate system associated with the source), we obtain, respectively, the values $m \approx 8.0 \times 10^9\, M_\odot$, $m \approx 1.0 \times 10^{10}\, M_\odot$. In this case, along with 3C 454.3, the blazar AO 0235 + 164 becomes one of the most massive SMBHs.

The satellites revolve in circular orbits around a common center of gravity. The orbital dimensions are close to each other and are: $R_{\rm comp} = 2 \times 10^{17}$ cm and $R_{\rm center} = 1.6 \times 10^{17}$ cm. The satellite orbital velocities will be respectively equal to $v_{\rm comp} \approx 1.7 \times 10^4$ km s^{-1}, $v_{\rm center} \approx 1.4 \times 10^4$ km s^{-1}. It should be kept in mind that the orbital period of 25 years is

taken in the coordinate system associated with the source. The resulting value of the satellite's orbital velocity even exceeds the velocity of matter in a Type I supernova explosion.

For example, at a satellite velocity of 1.7×10^9 cm s^{-1}, the temperature of the medium can increase to approximately 10^{10} K. The isotropization of plasma particle motion occurs behind the shock front. In this case, the directed motion of the shock wave is transformed into chaotic particle motion, determined by the plasma temperature $mv^2/2 = 3kT/2$. For hydrogen plasma, we obtain $T \approx 10^{10}$ K. For heavier nuclei, the temperature will be higher. In any case, the plasma temperature is above the threshold for the formation of electron-positron (e–n) pairs ($T \approx 5 \times 10^9$ K). Supersonic shock waves, with the dilution factor considered, reach the beginning of the jet and form plasma clumps with a magnetic field. The clumps consist of nodes (irregularities) of varying sizes. Near the beginning of the jet, electric and magnetic fields can accelerate plasma formations almost to the speed of light, forming, in addition to clouds of electron-proton plasma, 'jets' consisting of (e–e) pairs. At this time, the greatest activity can be observed in the gamma-ray range. This is a possible, but not directly proven, scenario.

Presumably, the orbits of the satellites intersect their common accretion disk (AD). In this case, its dimensions should exceed 10^{17} cm. The radius of AD can be estimated based on the formula for the precession of the central body in a SMBH binary system [32]:

$$T_{\rm pr} \approx 10^6 \left(\frac{M+m}{10^9 M_\odot}\right)^{1/2} \left(\frac{a}{10^{19}\,{\rm cm}}\right)^3 \left(\frac{a_{\rm d}}{10^{18}\,{\rm cm}}\right)^{-3/2} \times \left[\frac{(1+q)^{1/2}}{(q\cos\theta)}\right] {\rm years}, \quad (12)$$

where $q = m/M$, $a = r_{\rm comp} + r_{\rm center}$ is the distance between the satellites, $a_{\rm d}$ is the radius of AD, θ is the angle between the planes of the orbits and AD. Equation (12) can be transformed to a form convenient for calculating the radius of the accretion disk:

$$a_{\rm d} \approx 10^{22} \left(\frac{M}{10^9 M_\odot}\right)^{1/3} \frac{r_{\rm comp}+r_{\rm center}}{10^{19}\,{\rm cm}} (1+q)^{1/3} (T_{\rm pr} q \cos\theta)^{2/3} {\rm cm}. \quad (13)$$

Substituting the data for the precession period into Eqn (10) with $T_{\rm pr} \approx 75$ years (Table 2), we obtain data on the mass of the satellites $m \approx 6.0 M_\odot$, $M \approx 7.5 M_\odot$, the distances between them $a_{\rm (center+comp)} \approx 3.6 \times 10^{17}$ cm, $\theta = 0$ (the plane of the accretion disk and the orbit coincide), and q. The value of $a_{\rm d}$ will be: $a_{\rm d} \approx 2.3 \times 10^{18}$ cm. If we take the half-thickness of the accretion disk equal to the standard α-disk [33], then we have $a_{\rm d\,OJ287} \approx 0.07 a_{\rm d} \approx 5.6 \times 10^{17}$ cm, which is comparable to the size of the companion orbit ($r_{\rm comp} \approx 2.0 \times 10^{17}$ cm), but less than the distance between companions ($a_{\rm (center+comp)} \approx 3.6 \times 10^{17}$ cm). Thus, in this case, the AD cannot be called a physically thin disk.

Observations of X-ray binaries indicate a significant half-thickness of the accretion disks up to $h \approx 0.25 a_{\rm d}$. On the other hand, it is known that standard accretion α-disks have a significantly smaller half-thickness of $h \approx 0.07 a_{\rm d}$. Independent numerical methods have shown that their maximum half-thickness cannot exceed $h \approx 0.1 a_{\rm d}$. The most likely reason for the increase in the thickness of the accretion disks in the X-ray wavelength range is the presence of matter above the disk in the form of a hot corona, which scatters hard radiation from the central source and the inner disk. Observations of X-ray binaries indicate a significant half-thickness of the accretion disks up to $h \approx 0.25 a_{\rm d}$ [33–35]. Our data are free from this drawback of the X-ray wavelength range and do not contradict theoretical data on standard accretion α-disks.

Based on an analysis of observational data, it was suggested that the magnitude of the delays of flare events at different frequencies is a function of the angles between the direction of the ejections and the observer's line of sight [36]. The magnitude of the delay is related to the gamma factor and the angle between the ejection and the direction to the observer: $\gamma = 1/\theta$. According to observations of the 2009 flare, these angles in the case of AO 0235 + 164 should be 2.9°, which corresponds to a Lorentz factor of $\gamma \approx 20$. After this, the flare amplitude became progressively smaller. This could be associated with an increase in the angle between the ejection (the 'jet') and the direction to the observer.

2.4 Discussion

Over the past decades, several approaches to determining the parameters of binary SMBHs have been developed and successfully applied. One of the most widely used methods is the search for quasi-periodic variations in the luminosity of an object caused by the orbital motion of the components and the precession of the accretion disk. A striking example is the blazar OJ 287, in which a periodicity of flares with an interval of ~ 12 years is observed. This periodicity can be explained by the passage of the secondary black hole through an AD common with the primary BH, which allows modeling the orbit and estimating the masses of the components [37, 38]. Similar approaches were applied to the object AO 1302-102 [39], where a periodicity of about 5 years was observed according to data from the CRTS and LINESAR optical surveys.

In a number of cases, the observed changes in the direction of relativistic jets can be explained by the action of precessional forces arising from the interaction between two SMBHs [40, 41]. This method requires complex modeling of the jet structure based on VLBI observations.

Double or shifted broad emission lines have been detected in the spectra of some AGNs. Observing the Doppler shifts of broad emission lines in the spectra of AGNs makes it possible to determine the orbital motion of black holes. Changes in the profiles and positions of lines such as H_β and MgII are interpreted as a consequence of the motion of one of the components of the binary system [42–44]. Similar studies have been performed for objects SDSS J1536 + 0441, J 093201.60 + 031858.7, and others. However, this method is sensitive to the physical characteristics of the accretion disk, and alternative interpretations of the observed effects are possible.

For relatively nearby AGNs, direct observation of two cores is possible using VLBI observations. An example is the radio source 0402 + 379, for which a pair of active nuclei was detected at a distance of ~ 7 pc [45–47]. Such observations allow us to directly measure the distance between the components and estimate their masses. This method allows tracking the motion of individual components on subparsec scales. However, even with the most powerful global VLBI networks (e.g., VLBA, EHT), it is difficult to achieve the resolution necessary for directly imaging binary SMBHs at large cosmological distances.

The presence of a binary SMBH can cause jet precession, leading to its S-shaped or helical structure. Modeling such structures makes it possible to determine the precession period and draw conclusions about the orbital parameters. A similar approach was applied, e.g., to the objects 3C 345 [48], S5 1803 + 784, and 3C 273 [49]. Combining long-term radio observations with precession models provides important information about the dynamics of the systems.

Numerical hydrodynamic modeling of accretion in systems with two SMBHs allows us to reproduce the observed luminosity variations and emission morphology. Such models take into account perturbations caused by the secondary component, the formation of spiral waves in the accretion disk, and modulations of the matter flow. References [50, 51] demonstrated that the interaction between the components and the accretion disk shared by the SMBH leads to characteristic periodicities in the light curve and emission spectrum. A number of studies use modeling of accretion and relativistic hydrodynamics in binary systems to obtain synthetic light curves and jet maps [52]. Their comparison with monitoring data allows us to refine the model parameters: mass, orbital eccentricity, orbital radius, etc.

Some studies use time delay methods between signals in different ranges — e.g., between optical and X-ray — to reveal orbital effects and the structure of the accretion flow. Such methods require long, high-precision time series and statistical analysis, but can be effective when long observation series are available [53–56].

Summarizing the approaches, we can highlight a trend toward interdisciplinary synthesis: combining spectroscopy, radio interferometry, photometry, and numerical modeling. Combining multifrequency monitoring and interferometry methods appears particularly promising, as discussed in several recent studies [57, 58].

Existing methods for determining the parameters of binary SMBHs cover a wide range of observational and theoretical approaches. Each has its own limitations related to the distance to the object, the resolution of the observation equipment, and data availability. The most reliable results are obtained with an integrated approach combining several independent methods. In this context, the technique proposed in this paper — analyzing multi-frequency radio observation series using harmonic and wavelet analysis — is particularly valuable for studying cosmologically distant objects that cannot be directly resolved, such as 3C 454.3, S 0528 + 134, and AO 0235 + 164.

According to the results obtained, the SMBH binary AO 0235 + 164 is one of the most massive and dynamic systems. Its kinetic energy reserve is $E_{\rm kin} = E_{{\rm kin},M} + E_{{\rm kin},m} \approx 1.5 \times 10^{61}$ erg. This energy is expended on gravitational radiation, overcoming dynamic friction in the dense medium of the AD. The lifetime of the SMBH AO 0235 + 164 before merger [59]:

$$T_{\rm merger} \approx \frac{2 \times 10^{-2} c^5 R^4 (1-e^2)^{7/2}}{G^3 m M (m+M)}, \qquad (14)$$

where $R = R_{\rm comp} \approx 3 \times 10^{17}$ cm, $m \approx 6 \times 10^9 M_\odot$ and $M \approx 7.5 \times 10^9 M_\odot$ are the masses of the satellites, c is the speed of light, and $e = 0$ is the eccentricity of the satellite's orbit. From this, we obtain a merger time of $T_{\rm merger} \approx 4.6 \times 10^5$ years. By cosmic standards, this is very little. These data were obtained exclusively from radio observations, and the described method for obtaining them is applicable to all AGNs that have long multi-frequency series in different radio wave ranges.

The obtained results are consistent with those of other researchers, who also observed similar dynamics for systems with binary supermassive black holes. For example, Ref. [60] showed that systems such as AO 0235 + 164 can experience significant energy losses through gravitational waves, which accelerates their merger and changes their orbital parameters. In addition, analysis [61] based on spectroscopic data confirms the high kinetic activity of such systems, indicating the possibility of detecting gravitational waves using sensitive detectors.

We also calculated the rate of energy loss through gravitational waves [62]:

$$\left\langle \frac{{\rm d}E}{{\rm d}t} \right\rangle = \frac{32 G^4 M^2 m^2 (M+m)\left(1 + (73e^2/24) + (37e^4/96)\right)}{5c^5 a^5 (1-e^2)^{7/2}}. \qquad (15)$$

For the found values of the masses of the AO 0235 + 164 companions, the values of $a = R_{\rm center} + R_{\rm comp} \approx 3.6 \times 10^{17}$ cm and the eccentricity $e = 0$, we have $\langle {\rm d}E/{\rm d}t \rangle \approx 5.7 \times 10^{47}$ erg s^{-1}. The obtained value is one and a half times smaller than that of the most powerful GW emitter 3C 454.3 [4] and is comparable to the GW power from OJ 287 [63]. Considering that AO 0235 + 164 is located further than OJ 287, it is one of the leading candidates for detecting GWs. Our results on the AO 0235 + 164 emission power of $\approx 5.7 \times 10^{47}$ erg s^{-1} coincide with the data of other studies, such as Ref. [64], where similar results for the gravitational wave emission power were obtained for blazars such as OJ 287. This confirms that AO 0235 + 164 has a comparable emission power to other active galactic nuclei, which are promising candidates for detecting gravitational waves.

Currently, four blazars are known, presumably with known physical parameters. By parameters, we mean the precessional and orbital periods of the SMBH satellites, the orbital radius of the satellite, the masses of the satellites, and the lifetime before merger. These blazar characteristics are presented in Table 3.

The most massive system is the AGN 3C 454.3. The central object possibly has a mass of 24 billion solar masses. This object is also the shortest-lived, with a lifetime before merger of only 5.5×10^4 years. These results are also confirmed by studies [65], where similar calculations of the lifetime before merger were performed for the 3C 454.3 system, indicating its high dynamical activity.

This AGN is followed by OJ 287 in terms of the listed characteristics. The blazar AO 0235 + 164, which we analyzed, occupies the third place. Nevertheless, we conclude that the supermassive black hole AO 0235 + 164, as well as the supermassive black holes 3C 454.3 and OJ 287, are promising for detecting gravitational waves from it using the International Pulsar Timing Array (IPTA) gravitational wave detector, which operates at this ultra-low frequency and has the high sensitivity necessary to detect low power values near the Earth's surface [66].

One more important conclusion can be noted. For cosmologically distant sources such as 3C 454.3, S 0528 + 134, and AO 0235 + 164, it is impossible to establish the binarity of SMBHs using direct interferometric observations. This is confirmed by the results of Ref. [67], where it was shown for similar systems such as OJ 287 that existing methods do not allow resolving such components at cosmo-

Table 3. Physical parameters of 3C 454.3, S 0528 + 134, AO 0235 + 164, 3C 273. All periods are in years.

3C 454.3	Precessional period in the source coordinate system (T_{pr})	Orbital half-period in the source coordinate system (T_{orb})	Orbital half-period in the source coordinate system ($T_{orb}/2$)
	188 ± 19	31.0 ± 2.8	15.0 ± 1.5
Companion radius (cm)	Mass of the central SMBH ($M_\odot$)	Mass of the companions ($M_\odot$)	Lifetime of the companions before merger (years)
4.5×10^{17}	2.4×10^{10}	6.8×10^{9}	5.5×10^{4}
S 0528 + 134	Precessional period in the source coordinate system (T_{pr})	Orbital half-period in the source coordinate system (T_{orb})	Orbital half-period in the source coordinate system ($T_{orb}/2$)
	100 ± 10	52 ± 7.4	24 ± 3.4
Companion radius (cm)	Mass of the central SMBH ($M_\odot$)	Mass of the companions ($M_\odot$)	Lifetime of the companions before merger (years)
2.0×10^{17}	5×10^{9}	2.5×10^{9}	10^{5}
AO 0235 + 164	Precessional period in the source coordinate system (T_{pr})	Orbital half-period in the source coordinate system (T_{orb})	Orbital half-period in the source coordinate system ($T_{orb}/2$)
	72 ± 2.5	25 ± 1.5	12 ± 0.7
Companion radius (cm)	Mass of the central SMBH ($M_\odot$)	Mass of the companions ($M_\odot$)	Lifetime of the companions before merger (years)
2.0×10^{17}	7.5×10^{9}	6.0×10^{9}	4.6×10^{5}
3C 273	Precessional period in the source coordinate system (T_{pr})	Orbital half-period in the source coordinate system (T_{orb})	Orbital half-period in the source coordinate system ($T_{orb}/2$)
	287 ± 20	77 ± 5	38 ± 2.5
Companion radius (cm)	Mass of the central SMBH ($M_\odot$)	Mass of the companions ($M_\odot$)	Lifetime of the companions before merger (years)
4.5×10^{17}	1.0×10^{10}	0.55×10^{10}	3×10^{5}

logical distances. Indeed, the angular separation between the components of the SMBH source is about 10^{-5} seconds of arc, considering the distance to the object $R \approx 2 \times 10^{27}$ cm. Global interferometers cannot provide a resolution of 1–2 microseconds without reliable resolution of the binary system.

Thus, new approaches may be required to establish the binarity of such systems. One promising method is to use combined data, such as radio observations at various frequencies, including millimeter and optical wavelengths, to accurately determine the orbital parameters of satellites. We propose using our approach to analyze such objects, which could provide greater accuracy in establishing their binarity and understanding their internal dynamics.

Furthermore, our result regarding the blazars 3C 454.3, S 0528 + 134, and AO 0235 + 164, which confirms their status as promising candidates for gravitational wave detection, opens new horizons for further observations and research. Using modern gravitational wave detectors such as IPTA, it is possible to detect signals from these objects, leading to new discoveries in astrophysics and providing valuable information about the dynamics of SMBHs.

Standard accretion of matter onto a rapidly moving SMBH is unable to provide the observed luminosity. According to the Schwartzman formula (1971),

$$\frac{\mathrm{d}E}{\mathrm{d}t}_{\text{accretion}} \approx 2 \times 10^{33} \left(10^{-2} \frac{M}{M_0}\right)^{3/2} (10^{-1} v)^{-9/4} n^{1/2} [\text{erg s}^{-1}].$$

Substituting the values of $M \approx 2.4 \times 10^{10} M_\odot$, $n \approx 3 \times 10^{9}$ cm^{-3} and $v \approx 3 \times 10^{4}$ km s^{-1}, we obtain a luminosity of the order of $L_{\text{accretion}} \approx 3.4 \times 10^{40}$ erg s^{-1}. This value is 7 orders of magnitude smaller than the total observed luminosity of the quasar 3C 454.3, ruling out accretion as the dominant energy source.

The model proposed by us explains the energy release by the passage of the secondary component of the binary SMBH through the accretion disk of the primary black hole. This interaction is accompanied by bursts of electromagnetic and gravitational wave radiation. Thus, the energy source in the brightest AGNs is not accretion, but the kinetic energy of the companion and the gravitational interaction in the compact system.

2.5 Conclusions

(1) A model for calculating the parameters of binary SMBHs based on multi-frequency radio monitoring data is proposed. It has been successfully demonstrated for the active galactic nuclei 3C 273, 3C 454.3, S 0528 + 134, and AO 0235 + 164.

(2) The model parameters include determining the masses of the SMBH components, the sizes of their orbits, their velocities, the system's kinetic energy reserves, energy losses due to gravitational radiation, and the system's lifetime before merging.

(3) Based on the obtained physical characteristics of 3C 273, 3C 454.3, S 0528 + 134, and AO 0235 + 164, it is shown that these active galactic nuclei may be very massive and nearby SMBHs containing companions with virtually equal masses.

(4) It has been shown that massive systems such as 3C 273, 3C 454.3, S 0528 + 134, and AO 0235 + 164 may be powerful

emitters of gravitational waves in the range from $10^{-8}-10^{-9}$ Hz, which can be detected by the International Pulsar Timing Array detectors.

3. Giant water vapor flares based on the data of long-term monitoring of galactic kilomasers

3.1 Introduction

One of the central tasks of modern astrophysics, necessary for understanding the evolution of the structure of the Universe, is the study of the mechanisms of star formation. This process has a fundamental impact on the formation and evolution of galaxies, the chemical enrichment of the interstellar medium, and the dynamical evolution of cosmic objects. In contrast to continuous electromagnetic radiation, which is created by thermal and synchrotron processes, spectral lines are formed at specific frequencies due to quantum transitions in atoms and molecules. These lines are the most important diagnostic tools for studying the physical conditions in star-forming zones [68].

Within the Milky Way, star formation occurs predominantly in cold and dense molecular clouds, the temperature of which is on the order of 10–100 K. It is under such conditions that condensation of matter is possible, leading to the formation of protostars. These regions contain a large number of molecules, including CO, NH_3, H_2O, HCN, CH_3OH, etc., which emit in the far infrared and radio ranges. Due to this, spectral observations in these ranges provide information about the density, temperature, velocity of matter, and chemical composition of stellar nurseries [69, 70].

Particular attention is paid to maser emission, which is due to population inversion of the energy levels of molecules. To stably maintain the population inversion, external energy pumping, radiative or impact, is required. Masers are observed, for example, in regions of active star formation, the shells of stars in the late stages of evolution, and even in galactic nuclei [71].

The history of the study of the interstellar medium dates back to the 17th century: the term ‘interstellar medium’ was first proposed by Francis Bacon in 1626. However, systematic study only began in the 20th century, when molecular bands were discovered in the spectra of cool stars, planetary atmospheres, and comets in the 1930s [72]. A breakthrough in molecular line radio observations occurred in 1963, when the hydroxyl molecule (OH) line was first detected in the spectrum of the Cassiopeia A supernova [73]. Since then, molecular line radio astronomy has developed rapidly, especially with the advent of high-sensitivity radio interferometers such as ALMA and NOEMA [74].

Today, more than 4500 spectral lines are known, belonging to approximately 80 different molecular species, including organic compounds and amino acid precursors [75]. These observations allow not only refining star formation models but also studying the processes of chemical evolution of matter leading to the formation of planetary systems and, possibly, to the origin of life.

Modern theoretical and numerical models of star formation consider turbulence, magnetic fields, radiative feedback, and the influence of nearby massive stars. Combined with observational data, this makes it possible to construct increasingly accurate scenarios for the formation of stellar populations in different types of galaxies and at different stages of their evolution [76, 77].

The study of individual sources began from an intense source of molecular lines in Orion, in the discovery of which RT-22 in Simeiz was involved. As early as the 1960s and 1970s, the 22-meter RT-22 radio telescope, located in Simeiz (Crimean Astrophysical Observatory), made an important contribution to these studies. Due to its high sensitivity and spectral resolution, RT-22 became one of the first instruments in the USSR to record molecular spectral lines in the radio range. Subsequently, the research expanded, and by the end of the 1970s, it was discovered that very young stars undergo a period of evolution, and the connection between molecular clouds and star formation is very close.

A landmark event in the development of Russian radio astronomy was the world’s first intercontinental very long baseline radio interferometry (VLBI) observations of molecular lines in 1971. The system, which included the RT-22 in Simeiz and the 37-meter radio telescope in Haystack Observatory (USA), recorded emission in the water vapor line at a frequency of 22.235 GHz (the $6_{16}-5_{23}$ transition) [78]. This allowed achieving the angular resolution of ~ 0.1 mas, record-breaking for that time, making it possible to reveal the smallest spatial structures of maser sources in our Galaxy. One of the most important results of these observations was the discovery of a high-power flare in the W 49 complex, a region of intense star formation in the Perseus arm of the Galaxy. Rapid variations in the radiation flux indicated extremely small sizes of the maser zones, which was confirmed by high-resolution VLBI observations [78, 79]. It was also established that the sources of H_2O masers often form compact clusters structurally associated with young stars and their accretion flows [80, 81].

Today, the RT-22 radio telescope continues to play an important role in studies of star formation and molecular astrophysics. Up-to-date technical modernization has made it possible to observe virtually all the main classes of cosmic masers, including OH, H_2O, CH_3OH, and SiO masers [79, 82]. In addition, RT-22 enables spectral observations in the millimeter frequency range from 85 to 115 GHz, which covers the lines of many molecules, including high-energy and organic compounds [83, 84].

Programs of this kind are implemented only on a limited number of radio telescopes in the world, as they require a complex technical infrastructure: precision receivers, cryogenic cooling systems, highly stable heterodynes, and powerful software packages for spectral analysis and data correlation [85, 86]. Thanks to these capabilities, RT-22 remains a valuable tool in studies of the early stages of star formation, the physics of the interstellar medium, and the evolution of molecular clouds [79, 84, 87].

3.2 Observation and data processing methodology

Existing receiving devices on RT-22 were upgraded to increase their sensitivity and reliability. New receiving systems were created in new frequency ranges. The choice of new frequency ranges was dictated by both the objectives of observing the least studied maser sources and the importance of the astrophysical problems being solved. Both cryogenic and uncooled receivers with amplifiers on HEM transistors were used, which ensured the intrinsic noise temperature of the receiving systems T_n of about 30 K at a frequency of 1.6 GHz when operating in uncooled mode and T_n of about 10 K at a frequency of 4.8 GHz in the cryogenic mode. The noise temperature of the system at a frequency of 22 GHz in the cooled mode was $T_n = 22$ K. Continuing with traditional

observations, in which the radiation of the ground state $^2\Pi_{1/2}$ of the OH molecule was studied (frequencies 1.612 GHz; 1.665 GHz; 1.667 GHz; 1.720 GHz), a receiver for 4.8 GHz was created, which made it possible to study the radiation on transitions of the $^2\Pi_{3/2}$ state. Until the turn of the last millennium, observations of maser sources in the 1.35-cm water vapor line were conducted using equipment for very-long-baseline interferometry.

In 2000, a new 1.35-cm receiver, manufactured at the Crimean Astronomical Observatory, was installed on the 22-meter RT-22 radio telescope. Beginning in 2002, a cryoelectronic radiometer cooled to hydrogen temperature (15 K) operating at 22 GHz and a parallel-type Fourier spectrum analyzer were developed and commissioned. The introduction of the parallel-type Fourier spectrum analyzer significantly increased the frequency resolution and made it possible to conduct systematic and comprehensive studies of star-forming regions. Further developments in 2009 included the introduction of a receiver with a frequency resolution of 0.5 kHz based on a parallel-type Fourier spectrum analyzer for spectral-polarimetric observations of maser sources in the water vapor line.

Measurements of the radio telescope-radiometer system parameters were conducted using the Mark-5B+ recording system and software developed in the Crimean Radio Astronomy Laboratory [88–91]. The system noise temperature was determined using sources with known fluxes in this range: DR 21, Vir-A, Cyg-A, and Tau-A. The influence of the source angular size on the main lobe width of the directional pattern was also considered. Before each measurement of the system's noise temperature, the accuracy of pointing to the source was determined by scanning in two directions (alpha and delta). The radio telescope was then alternately positioned on the radio source and on a point located away from it (source — background).

3.3 The most powerful galactic kilomaser G25.65+1.05 (IRAS 18316-0602)

The source IBA8 18316-0602 was not outstanding in the IRAS catalog, so it initially did not attract much attention from researchers. The super powerful flares that occurred in IRAS 18316-0602 at the end of 2016 and from September 2017 to February 2018 (Fig. 6) forced the researchers to change their attitude toward it and consider how such an ordinary source could increase the flux in the water vapor line to almost 1.3×10^5 Jy, i.e., almost thousandfold.

The water vapor maser (transition $6_{16}-5_{23}$) in the infrared galactic source IRAS 18316-0602 was discovered in March 1989 during a survey of a sample of objects from the IRAS Point Source Catalog (PSC), selected according to certain criteria. The work was carried out at the 32-m radio telescope in Medicina (Italy) by a group of researchers who observed 260 infrared sources and detected H_2O masers in 17% of them. Most of the masers were new, including the maser IRAS 18316-0602 [92]. At the time of discovery of IRAS 18316-0602, its integrated flux in the H_2O line was $F_v \approx 1000$ Jy.

At RT-22, the source was observed sporadically since 2000, but more regular observations began in early 2017. No significant increases in the radiation flux density were recorded in the object. Figure 6 shows the flux density in the water vapor line depending on the observation epoch. Most of the plotted data is published in Refs [92, 93] (marked with crosses), while the data of our observations

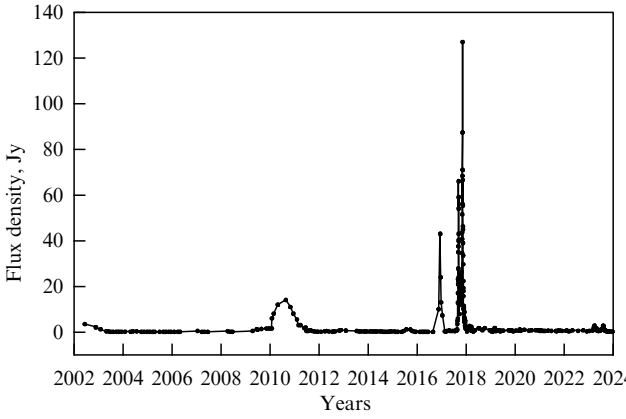

Figure 6. Long-term monitoring of IRAS 18316-0602 in the water vapor line.

are marked with circles. Figure 6 shows that three isolated large flares with increasing amplitude occurred during the period from 2000 to August 2017. Although the maximum of the 2002 flare could not be fully recorded, it is clear that it was smaller than the subsequent maximum of 2010–2011. The flares of late 2016 were larger in amplitude than the two preceding ones [93].

Along with the increase in flare amplitude over time, a reverse trend in flare duration is observed. The duration of the 2002 flare was approximately 2 years. The duration of the 2010–2011 process has halved to one year. The flux surge at the end of 2016 has shrunk to one month. It cannot be ruled out that we are dealing with different objects, flaring in 2002, 2010–2011, and 2016.

If we assume the existence of a quasi-period based on observational data from long-term monitoring of the H_2O maser amplitude, it will be $T_{\rm per} \approx 7-8$ years. However, the amplitude of the superflares that outline this period varies by an order of magnitude, increasing over time. It is not easy to identify a physical process, separated in time by 15 years (the time between the first and third superflares), that would explain the presence of such a dependence of the amplitude on time:

$$\log\left(\frac{A_2}{A_1}\right) \approx k \log \Delta T, \tag{16}$$

where A_2/A_1 is the ratio of the amplitudes of the subsequent and previous flares, ΔT is the time between flares in years, and $k \approx 0.5$ is a constant.

Since the beginning of the last flare of the water maser in IRAS 18316-0602 in September 2017, we have monitored the object, in most cases, daily (Fig. 7) [94, 95]. The spectral flux density variation curve is double — humped. This shape may indicate abrupt changes in the physical characteristics of the water vapor maser emission regions, including those associated with a sudden energy injection. The shape of the flux density variation curve with time (exponential increase and decrease in flux, as well as binarity) rules out the explanation of the flare phenomenon by the radiation pattern effect. Therefore, this hypothesis explaining the variability of the water vapor maser flux density should be abandoned.

A distinctive feature of the recent giant flares in IRAS 18316-0602 is also their durations, which are noticeably shorter than the duration of the first two flares (Fig. 6).

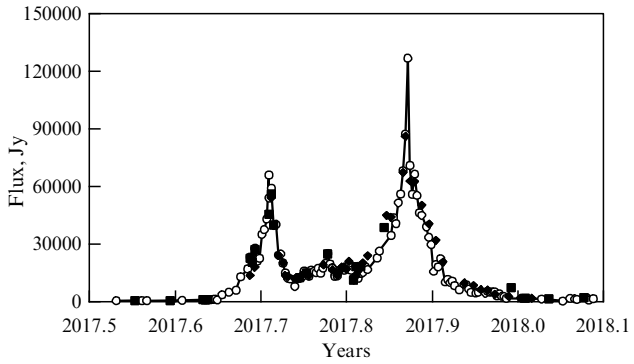

Figure 7. Double flare of maser emission in IRAS 18316-0602. Circles represent data from RT-22 Simeiz, squares represent data from HartRAO, and diamonds represent data from Torun.

The total duration of the 2017–2018 double flare and the flare of late 2016 (15 months) is comparable with the duration of the 2010–2011 flare. If the source of the flares is the same, this may be due to the fact that the data collection rate in the first two superflares was extremely low. The 2010–2011 flare is indicated by seven points, and the 2002 flare by only three. With such a duty cycle of observations, when data collection was carried out at intervals of 2–3 months, visually one may get the impression that we are dealing with several flares that have merged, when the processes of maser deactivation gave way to processes of its activation between data collections (see Fig. 6). However, it is possible that powerful bursts of the water vapor maser in IRAS 18316-0602 have been occurring since 2002 with increasing amplitude in accordance with relation (16) and were activated by different sources.

The giant flare of the water vapor maser in G 25.65 + 1.05 (IRAS 18316-0602), which occurred in September 2017–February 2018, was the fourth and most powerful in the history of observations of the source. Detailed temporal monitoring of the flux density during a flare allows important conclusions to be drawn regarding the analysis of the flare shape.

The shape of the flares is not symmetrical. The slopes of the double flare can be approximated by an exponential dependence (Fig. 7). The exponential shape of the maser flux density curve serves as a key indicator of the maser state during the flare — it operates in an unsaturated mode, when the maser gain increases exponentially with increasing pump rate [96].

The shape of the central part of the maser line near the maximum phase (decreasing to 50 kHz) suggests a single-component source responsible for the most part of the flux density increase. Samples of water vapor line recordings in IRAS 18316-0602 near the maxima of the first and second flares of 2017–2018 are shown in Fig. 8.

At flare slopes below 20,000 Jy, it becomes clear that the object emitting the water vapor line is not single-component, but rather consists of at least two components, one of which is activated to a lesser degree. An example of a line recorded in flares up to 20 kJy is shown in Fig. 9.

Figure 7 (constructed, like all subsequent figures, based on the flux density maxima in the line) clearly shows the second component of the flare, which is bell-shaped. The total duration of this component is 4 months. Its onset was in early September 2017. The end of this flare component was the end of 2017. The amplitude of the flare component (20 kJy) exceeds the amplitude of the flares of 2002 and 2010–2011 in accordance with expression (1). Therefore, it can be con-

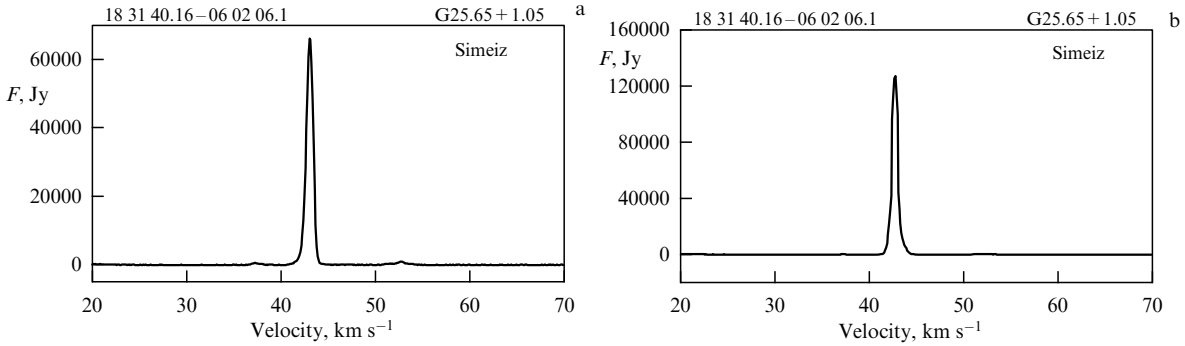

Figure 8. Example record of the water vapor line in G25.65 + 1.05 (IRAS 18316-0602) at the maximum: (a) of the first flare, (b) of the second flare (2017–2018).

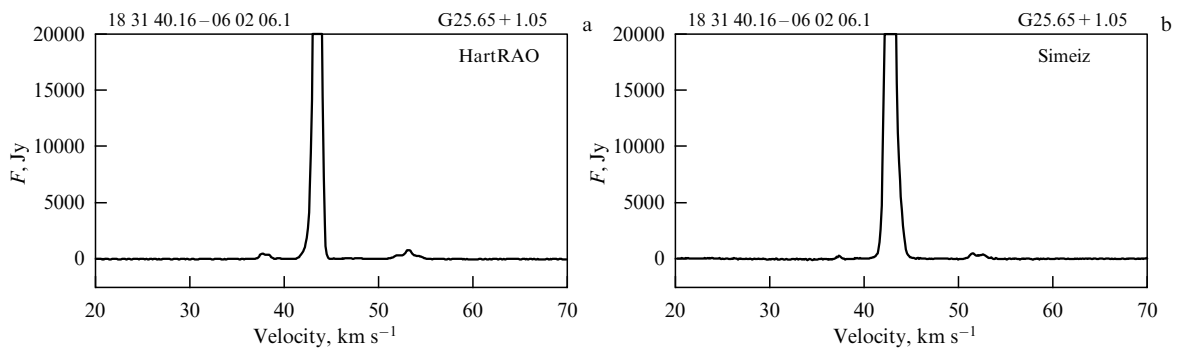

Figure 9. Example record of the water vapor line in G25.65 + 1.05 (IRAS 18316-0602) up to 20 kJy at the maximum: (a) of the first flare, (b) of the second flare (2017–2018).

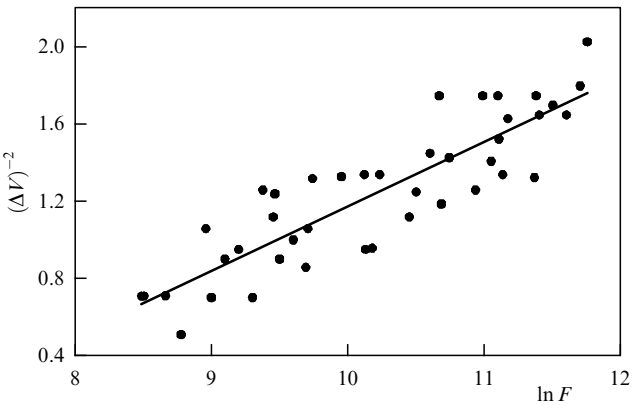

Figure 10. Dependence of the water vapor maser line width on the flux during the flare in G25.65 + 1.05 (IRAS 18316-0602) in September 2017–February 2018.

cluded that the bell-shaped source of the 2017–2018 flare in IRAS 18316-0602 is identical to the one that was in the flares of 2002 and 2010–2011, but the flare amplitude (20 kJy) is one and a half to two times greater than the amplitude of the 2010–2011 flare.

It is also clear that the narrow double exponential maser flare of 2017–2018, like the flare of late 2016, has a different nature from the flares of 2002 and 2010–2011. This is clearly visible in our double flare, which combined both sources of all previous flares. An additional distinctive feature of the 2017–2018 flare is its dual nature.

As in the case of the 2016 flare [Lekht E.E., Pashchenko M.I., Rudnitskii G.M., Tolmachev A.M. *Astron. Rep.* **62** 213 (2018); https://doi.org/10.1134/S1063772918030071], in the flare of 2017–2018 under consideration, a dependence of the line width on the amplitude of the flare phenomenon is observed.

In coordinates ($\ln F$, ΔV^{-2}), this dependence is presented in Fig. 10, where F is the flux density at the line maximum in jansky units, and ΔV is the line width at half-maximum level in km s^{-1}. The experimental data are plotted as dots. The plot is approximated by a straight line. At the activity maximum, the line is strictly symmetrical and is perfectly described by a Gaussian.

This also indicates that the maser is in an unsaturated state. The data, however, are not clearly expressed. Similar results were obtained for the giant flare in Orion KL [97, 98], where it was concluded that the maser is in an unsaturated state up to nearly the maximum flare amplitude.

It should also be noted that the maser line radial velocity for the two considered different components of the 2017–2018 flare is practically the same and equals about 42.8 km s^{-1}. This means that the emission zones must be located at a close distance. Nearby maser globules emit a maser line at close radial velocities, but the characteristics of the line amplitude change are different. It is not entirely clear how a single external maser pump source can operate in such different ways. Apparently, the explanation should be sought in the differences in the characteristics of the maser globules, which emit in different ways, creating a difference in the amplitude and duration of the flare.

The gigantic amplitude of the flare (approximately 130 kJy) and the distance to the source (12.5 kpc) make kilomaser IRAS 18316-0602 the most powerful in our Galaxy. As with W49, a single star of at least class O5, and possibly O4, is required as the primary energy source to provide the observed infrared luminosity. Multiple stars at the center of the nebula could also provide the observed infrared luminosity, with the class of the most massive star being O5. These are among the most massive stars in the Galaxy.

Linear polarization measurement in IRAS 18316-0602.

In accordance with the adopted observation methodology, on September 17, 2017, during the first maximum phase of the binary flare of IRAS 18316-0602, its linear polarization in the water vapor line was measured. For each rotation of the polarizer polarization plane by a fixed angle, the radiometer output signal was integrated for 3 min using a spectrum analyzer. Observations were made in the meridian, so the resulting position angle of the amplitude maximum corresponds to the position angle of linear polarization in the source, which is $-22°$.

The linear polarization value was calculated using the formula:

$$P\,\% = \frac{P_{\max} - P_{\min}}{P_{\max} + P_{\min}}\,, \tag{17}$$

where $P_{\max}$, $P_{\min}$ are the maximum and minimum flux density in linear polarization, respectively.

The maximum linear polarization value was approximately 30%, which is almost half the maximum linearly polarized radiation flux during powerful flares in such well-known kilomasers as W49 and Orion KL. Thus, at the Orion KL during the giant flare of the water vapor maser in 1980, the percentage of linear polarization reached almost 60% [99, 100]. The linear increase in the percentage of polarization with increasing flux density of the H_2O maser by hundreds of times to the level in the 1980 flare is an indicator of an unsaturated maser operating at the Orion KL, in which stimulation of the emission velocity predominates, and the maser gain increases exponentially with the pumping rate [96]. With increasing flux density in the 1980 flare from 10^6 Jy to a maximum value of 2.2×10^6 Jy, the percentage of polarization remains unchanged. In this case, the maser gain increases linearly with the pumping rate, and the maser becomes saturated.

In the case of the source IRAS 18316-0602 during the 2017–2018 flare, the percentage of linear polarization is half that in Orion KL during the 1980 superflare. Therefore, it is natural to assume that the maser in the source IRAS 18316-0602 was in an unsaturated state during the flare of September 2017–February 2018. This is an additional argument in favor of the unsaturated state of the water vapor maser in IRAS 18316-0602, in addition to the exponential shape of the flux density variation curve.

In addition, evidence in favor of the unsaturated state of maser amplification is provided by the behavior of the line width of the water vapor maser. According to the maser line profile model [101], in the case of an unsaturated maser, the line width decreases with increasing flux density according to the law:

$$\log P = A + B\Delta v^{-2}\,, \tag{18}$$

where $P_{\max}$ is the flare flux density, Δv is the linewidth of the water vapor maser during the flare. Observational data do not contradict this relation, but the accuracy does not allow for unambiguous conclusions.

Thus, during the double hyperflare of the water vapor maser in IRAS 18316-0602 in 2017–2018, we have the basic conditions for the existence of an unsaturated maser. As the flux density increases, its exponential growth is observed [102, 103]. This occurs for both the first and second flares. Then, an exponential decrease in the flux occurs, also in both flares. A moderate percentage of linear polarization was measured at the maximum of the flare flux density.

Interferometric observations.

Interferometric experiments to observe IRAS 18316-0602 were performed in September 2017 as a series of six consecutive daily sessions on the interferometer, which included three 32-m radio telescopes of the Kvazar-KVO VLBI complex and a 22-m radio telescope — the Simeiz VLBI station [103]. In the VLBI observations, the start of the band was set at a frequency of 22229 GHz, and the duration of scans of the source under study was 20 minutes. The source 3C 454.3 was chosen as the calibrator, which was observed with scans of 5 or 20 minutes at the beginning, middle, and end of the session. Correlation processing of the VLBI observation data was performed using the DiFX 2.4.1 software correlator at the IAA RAS on a hybrid blade server cluster. Figure 11 shows a map obtained on September 27, 2017, when the source was in the phase after passing the first of the double flux density maxima.

In the map shown, 1 mas corresponds to a linear scale of approximately 20 au. This scale was obtained assuming a distance to the source of 12.5 kpc. At this resolution, it is difficult to distinguish individual globules, but the overall pattern of the radiation distribution in this region is quite clear. A bright central feature is visible, which is naturally associated with the globule (or compact globules) in which a uniquely powerful water vapor maser flare occurred. All other features are significantly smaller in amplitude.

The achieved resolution does not allow us to distinguish two components of the emission associated with two flares of different shapes: one of which is the central feature in Fig. 7, and the other is bell-shaped and has a smaller amplitude. Nevertheless, the interferometric data confirm our conclusions that the different globules responsible for different parts of the flare shape are close to each other and are located in a compact region. The obtained data do not contradict the results of observations of other outstanding galactic sources of maser emission, according to which the compact H II regions have dimensions of $l_{\mathrm{HII}} \approx 10^{16}$ cm [103]. Consequently, the molecular disks where maser globules may be located have dimensions of the order of $l_{\mathrm{disc}} \approx 10^{17}$ cm ($\approx 10^4$ au) and more.

It can be concluded that the interferometric data obtained during the flare of the water vapor maser in IRAS 18316-0602 confirm the presence of compact globules responsible for the powerful increase in the radiation flux density in this source.

Submillimeter data obtained in connection with the observation of the water vapor maser in IRAS 18316-0602.

Observations of the galactic source G25.65 + 1.05 (IRAS 18316-0602) were carried out at a wavelength of 870 μm near the maximum of the first flare of the water vapor maser on September 15–16, 2017, under favorable weather conditions, using the large bolometric camera 'APEX' [103].

The telescope focus was optimized using the planet Saturn, and pointing corrections were determined using the nearby point source J 1743-038. Saturn, the hot molecular

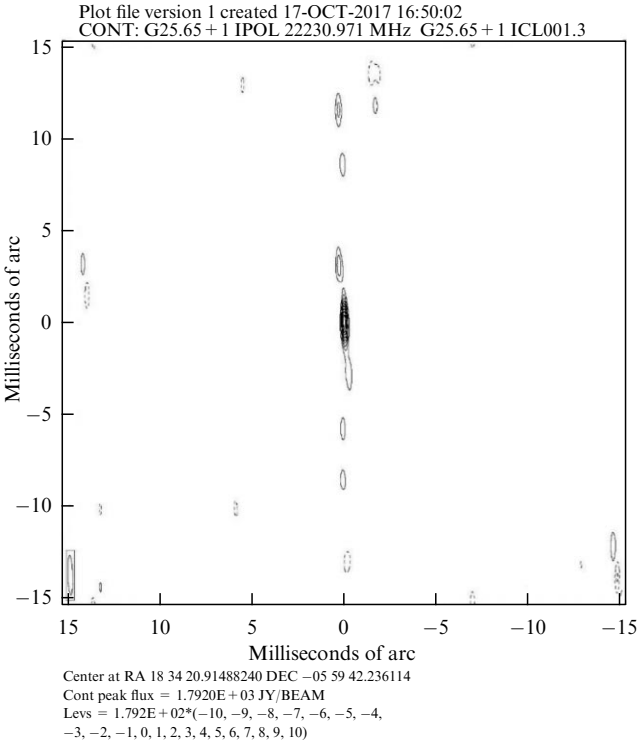

Figure 11. Interferometric image of IRAS 18316-0602 obtained based on the KVAZAR-Simeiz on September 27, 2017.

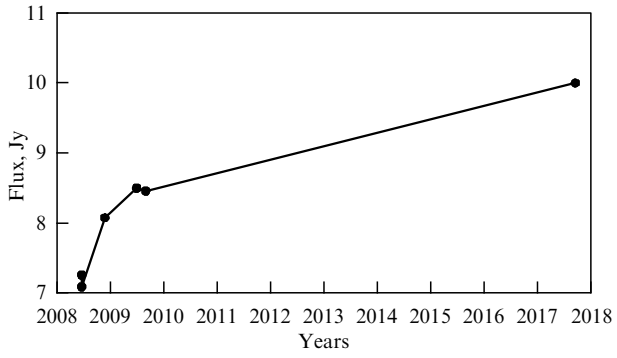

Figure 12. Long-term changes in the radiant flux density from G 25.65 + 1.05 (IRAS 18316-0602) at a wavelength of 870 μm, obtained using the large bolometric camera 'APEX.'

nucleus G34.26 + 0.15, and 10.62-0.38 were used as flux calibrators. Two of these galactic sources were observed on both days before and after G25.65 + 1.05.

Long-term variations in the flux density of G25.65 + 1.05 at a wavelength of 870 μm are shown in Fig. 12. During observations of this source, from 2008 to 2018, the spectral flux density increased by 40%, from 7 Jy to 10 Jy. Half of this increase occurred by the time of the 2010 flare (up to 8.5 Jy), the other half (up to 19 Jy) was recorded during the first (double) flare of 2017 (September 15–16, 2017).

The source submillimeter flux, which is an extension of the infrared emission, changed by tens of percent during the water vapor maser flares. This observational fact may indicate that the primary source of the activity may be a central massive star, hidden from our view by gigantic absorption in the optical wavelength range, which can amount to even hundreds of stellar magnitudes.

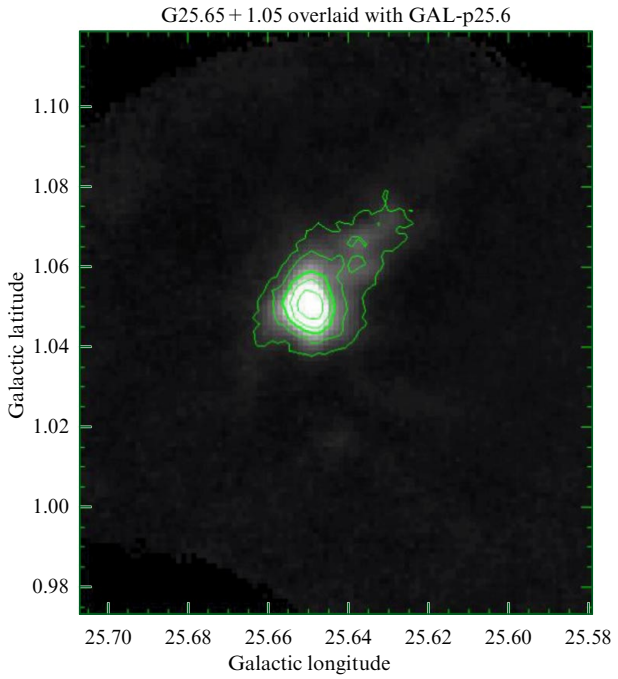

Figure 13. Image of G25.65 + 1.05 (IRAS 18316-0602) obtained at a wavelength of 870 μm with the large APEX bolometric camera.

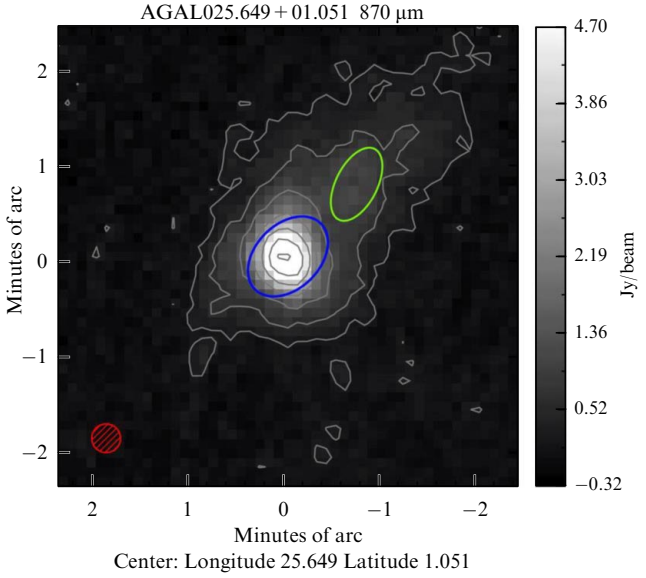

Figure 14. Image of G25.65 + 1.05 (IRAS 18316-0602) from the ATLASGAL catalogue.

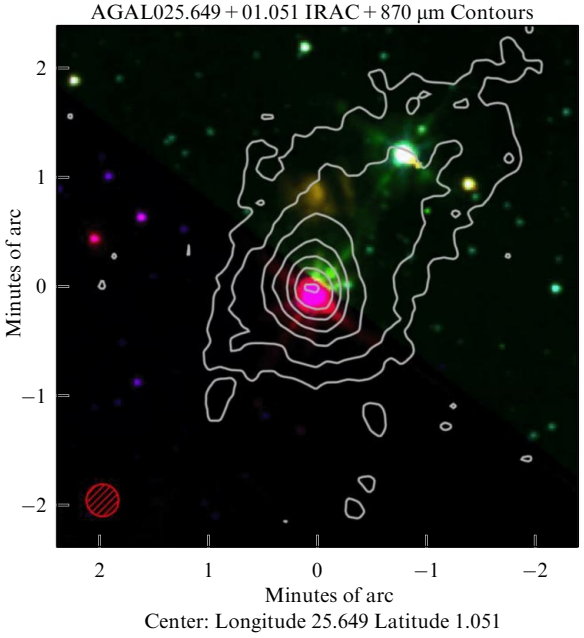

Figure 15. Image of G25.65 + 1.05 (IRAS 18316-0602) in the middle part of the infrared range (3.5, 4.6, 5.8, 8.0 μm).

An important question is whether the increase in the submillimeter flux preceded the onset of the water vapor maser flares. Judging by the plot in Fig. 12, it did. We see that by the beginning of 2010, the flux had already increased to 8.5 Jy and reached a local maximum. This was the beginning of the 2010–2011 water vapor maser flare. Unfortunately, submillimeter observations are not available until September 2017, when a very powerful flare occurred, at the maximum of which the spectral density of the submillimeter flux was already 10 Jy.

Thus, we can summarize that the increase in the submillimeter flux, and possibly the IR flux with it, is associated with maser flares, accompanying them, or even preceding them.

Figure 13 shows a map of the source G25.65 + 1.05 (IRAS 18316-0602), obtained with a large bolometer camera in September 2017 during a maser flare.

Figure 14 shows a map of G25.65 + 1.05 (IRAS 18316-0602) obtained as a fragment of the ATLAS-GAL catalog. The map resolution is given by the red circle in the lower left corner of the figure. The size of the source and its orientation are determined by the blue ellipse. The localization of other sources found in the survey of the galactic plane is shown in green. The image size is 5 × 5 arcminutes. The accuracy of the coordinates in the catalog does not allow comparing the coordinates of the source with the interferometric positions. The coincidence of the coordinates can be stated at the level of several arcseconds. This corresponds to tens of thousands of au taking into account the distance to G25.65 + 1.05 (IRAS 18316-0602).

Figure 15 shows an image of G25.65 + 1.05 (IRAS 18316-0602) obtained in the mid-infrared range using IRAC bandpass filters (3.5, 4.6, 5.8, 8.0 μm). The data are taken from the GLIMPSE Legacy Project. The image resolution is shown by the red circle in the lower left corner of the figure. The source is located in the center of the map. Within the coordinate errors, the positions of the submillimeter and IR sources coincide, which does not contradict the physical conditions that are realized in young galactic objects.

Figure 16 shows an image of G25.65 + 1.05 (IRAS 18316-0602) obtained in the mid-infrared range using IRAC bandpass filters (3.4, 4.6, 12, 22 μm). The data were obtained from the GLIMPSE Legacy Project. The image resolution is shown by the red circle in the lower left corner of the figure. The source is located in the center of the map. The maps obtained in the IR range correspond to each other.

3.4 Kilomaser in W51M

W51 is located in the Giant Molecular Cloud (GMC) of the Sagittarius spiral arm of the Milky Way [104]. Among giant molecular clouds, this is one of the few with a mass greater

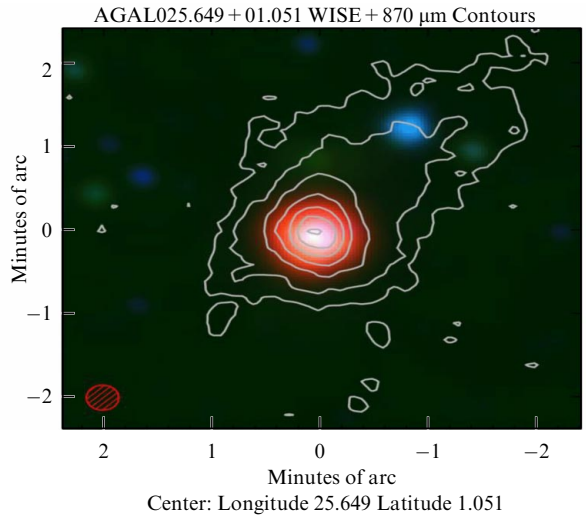

Figure 16. Image of G25.65 + 1.05 (IRAS 18316-0602) in the middle part of the infrared range (3.4, 4.6, 12, 22 μm).

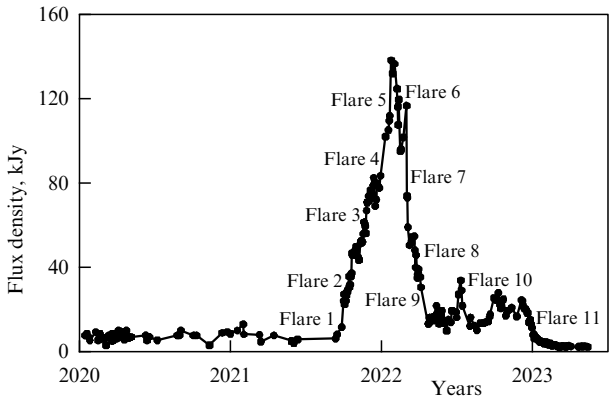

Figure 17. A powerful water maser flare event near 60 km s^{-1}. Individual flares are numbered.

than $10^6 M_\odot$ [105]. When mapped in the continuous spectrum, W51 has a complex structure. High-resolution observations within a second of arc revealed three separate components: W51 IRSI, W51 Main, and W51 IRS2. The location of these structures with their parts in different wavelength ranges is shown in Ref. [106]. Observations revealed the presence of a number of formed O stars and massive protostars associated with these components of W51 [107, 108]. Based on trigonometric measurements of W51 Main/South parallax, its association with a giant H II region was established, and the distance to the object was about 5 kpc [109].

The results of long-term monitoring of a water maser at a feature near 60 km s^{-1} in the direction of W51 Main are presented in Fig. 17. Data collection intervals were typically 1–2 days over the entire observation period from January 1, 2020, to June 7, 2022 [110]. The flare event was the most powerful in the entire history of source observations, both in terms of duration and flux density values. In terms of radiation power, this source is on a par with the galactic kilomaser W49N, given the amplitude of the event, equal to 140 kJy, and the distance to W51. Thus, it can be assumed that a new kilomaser has been discovered in the Galaxy.

The complex flare event consisted of many individual short flares, partially overlapping each other in time. The main flare activity lasted for a year and a half, from September 2021 to February 2023. The numerous flares that form the overall picture of the phenomenon apparently originated in a maser cluster, the size and density of maser spots in which are quite impressive. According to a preliminary conservative estimate, the cluster size is approximately 10–20 au. This is based on the assumption that maser spots are 0.5–1 au in size, leading to the conclusion that the cluster contains hundreds of maser spots.

By monitoring water maser observations with a single radio telescope, we can only record time-varying flux densities and radial velocities of spectral lines. In other words, we are capturing a dynamic picture of the source spectrum. Therefore, an optimal study requires the use of a comprehensive spectral-temporal method. We need to simultaneously analyze flux density monitoring data and spectral data. Then it becomes possible to understand the dynamics of the processes occurring in the active centers of maser formation.

The powerful flare event began with a sharp increase in the water maser flux density. This was associated with the appearance of a very short Flare 1, lasting only a few days and with an amplitude of about 25 kJy. Flares 1–5, each successively increased exponentially in amplitude, reached the maximum of the flare event. All flares 1–9 likely arose from maser spots located in a very compact region, since they were simultaneously close to the observer's line of sight. It seemed that the agent that initiated the appearance of water masers successively passed through maser spots densely 'packed' into a small cluster. Knowing the propagation velocity of this agent and the duration of the flare, we can determine the sizes of the cluster and individual maser spots independently. Below, in the discussion section, we will attempt to make approximate estimates of these quantities.

Having reached its maximum, the flux density of the flare phenomenon drops exponentially with each subsequent Flare 6–9 to a level of about 15 kJy [110]. The flare phenomenon then continues with the appearance of individual short flares until February 2023, when it ends with a drop in flux density to a background value of a few kJy. In the subsequent period of the flare phenomenon (September 2022–February 2023), the most significant were Flare 10 with an amplitude of about 35 kJy and Flare 11, which reached an amplitude of 30 kJy and consisted of several individual flares of smaller amplitude and duration (see Fig. 17).

Including spectral consideration in the analysis allows us to advance our understanding of the physical picture of maser emission generation [111]. For a maser in an unsaturated state, an exponential increase and decrease in the flux density during a flare, as well as a decrease in the line width with increasing flux density, are predicted [112]. Such a dependence for Flares 1–5 is shown in Fig. 18. The dependence is linear if it is represented as the ratio of the reciprocal of the square of the half-width of the spectral line to the logarithm of the flux density [113]. Its shape and slope indicate that short Flares 1–9 most likely belong to a water maser in an unsaturated state. The obtained slopes are close to each other and the dependence is practically a single whole with the possible exception of Flare 1. In this case, the range of flux density variation is about 120 kJy — from 20 to 140 kJy. The line widths varied from 0.4 to 0.6 km s^{-1}. Confirmation of the unsaturated state of water masers for Flares 1–9 can be seen from the flux density monitoring, plotted in natural logarithms of the flux densities (Fig. 18b).

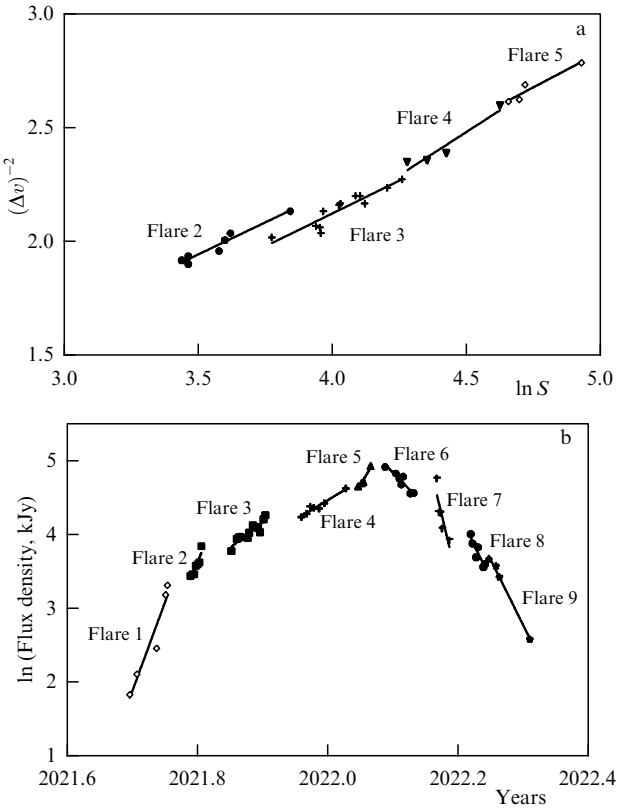

Figure 18. (a) Relationship between the spectral line width to the power of minus two $(\Delta v)^{-2}$ km s^{-1} and the natural logarithm of the flux density ln (S) kJy for Flares 1–5. (b) A powerful water maser flare event near 60 km s^{-1}. The flux densities of Flares 1–9 are plotted on a scale of natural logarithms.

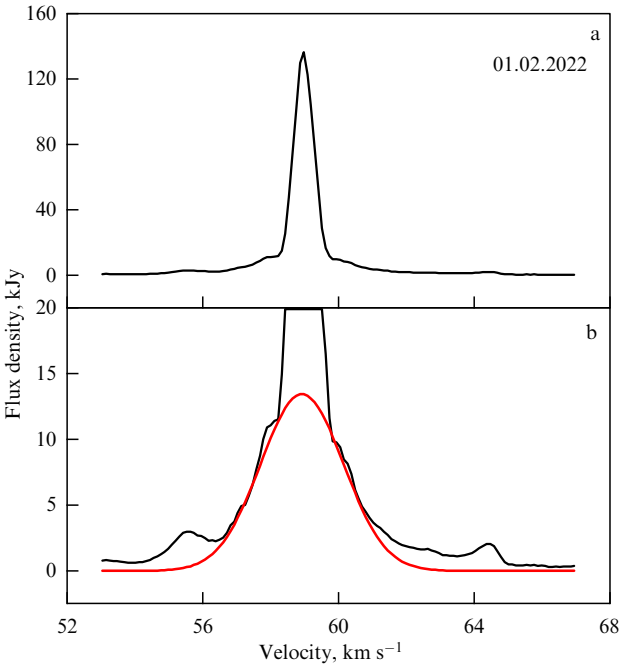

Figure 19. Spectra of features near 60 km s^{-1} for Flare 5 (a) and Flare 0 together with Flare 5 (b). Gaussian fit of Flare 0 ((b), red line). The amplitude of Flare 5 in Fig. b is limited by the flux density level of 20 kJy, at which Flare 0 is more clearly visible.

Another important conclusion is that each previous flare creates an input flux density for the subsequent one, in addition to the flux density generated by Flare 0 for all Flares 1–9 (Fig. 19). Flare 0 is overlapped by Flare 5, so we will not see the shape of Flare 0 inside Flare 5. The visible wings of Flare 0 allow us to construct a Gaussian approximation of it, and nothing more. All this suggests that the appearance of super-powerful water maser flares requires very large input flux densities into the maser condensations in which these flares occur. This means that the input flux densities to each maser condensation are formed not only by the long Flare 0, but also by all previous flares for all subsequent flares, which partially overlap each other. Moreover, since Flare 0 alone has a flux density of about 15 kJy, even this is a very high flux density. We have not yet seen such large input fluxes in any maser source.

The long Flare 11, which lasted from August 2022 to January 2023, was a set of several (3–4) subflares, the first of which had an amplitude of more than 30 kJy. After the end of Flare 9, a substantial level of maser activity of at least 13 kJy was observed, below which the flux densities of Flares 1–10 did not fall [110].

The half-width of the spectral line of the Flare 0 is approximately 3.0 ± 0.2 km s^{-1}. The formula for expressing the kinetic temperature is given in Ref. [112]:

$$T_{\mathrm{k,H_2O}} = \frac{\Delta v^2_{\mathrm{H_2O}}\, m_{\mathrm{H_2O}} c}{8k \ln 2}\,, \qquad (19)$$

here $\Delta v^2_{\mathrm{H_2O}}$ is expressed in (km s^{-1})^2, $m_{\mathrm{H_2O}}$ is the mass of a water molecule, c is the speed of light, and k is the Boltzmann constant. From Eqn (19) it follows that $T_{\mathrm{k,H_2O}} \approx 3100 \pm 200$ K. The uncertainty in the Gaussian approximation is included in the error. Thus, an unprecedentedly high value of $T_{\mathrm{k,H_2O}}$ was obtained for maser flares over the entire observation period of the source.

Before and after the flare event, its spectral characteristics changed mainly due to a decrease in the flux densities of the radial velocity components of individual flares (Fig. 20). Flare 0 has a significantly smaller amplitude than at the maximum. The drop in flare amplitude may be associated with a decrease in the density of the medium and/or the degree of ionization. This can occur at the edge of maser condensation, where the density of the medium is lower. The preservation of a high value of $T_{\mathrm{k,H_2O}}$ during Flare 0 (for more than a year) is a very important result.

It will be useful to analyze the dynamics of changes in the radial velocities of the flares involved in the creation and development of the flare event. Examining Fig. 19b and comparing it with Fig. 20, one can see that individual flares in Fig. 19 are also present in Fig. 20. This also applies to weak flares near radial velocities of 56, 60, and 64 km s^{-1} in Fig. 17. Moreover, the amplitudes of these flares did not even significantly decrease by the end of the flare event. To summarize, it can be noted that by the end of the flare event, Flare 0 had decreased in amplitude by approximately a factor of three. This can be explained by the fact that the agent initiating Flare 0 was located at that time at the boundary of the maser spot in which this flare occurred. When passing into a lower density medium, the velocity of the shock waves increases, which leads to an increase in the temperature of the medium ($v \sim T^{1/2}$). Therefore, some broadening of the saturated maser characteristic may become apparent.

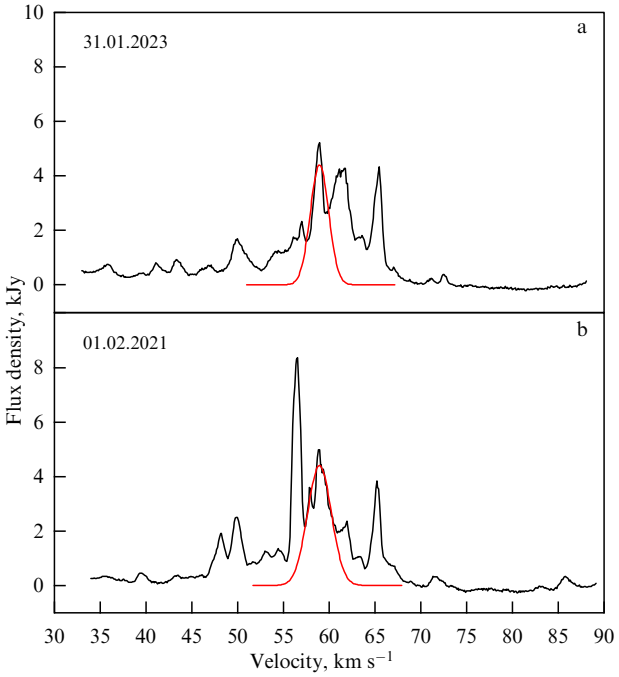

Figure 20. Spectra of features near 60 km s^{-1} for Flare 0 and background flares ((a) before the flare event and (b) after the flare event).

Two years passed between the spectra of Flare 0 before and after the flare event. The similarity of the parameters of Flare 0 in these two cases may indicate that the region of origin of Flare 0 may be located outside the maser cluster, where the maser spots responsible for the occurrence of Flares 1–9 are located. This region may be a halo of gas and dust in which a disk containing a maser cluster is immersed. If the agent responsible for the occurrence of shock waves is the same, then with a lower density of the medium and its larger dimensions, the temperature and saturation of the maser will be higher. Considering that Flare 0 is present during the entire period of increased activity, which is about three years, the size of the gas and dust disk in which the maser condensations are located can be estimated, responsible for Flares 1–9. With the velocity of the agent initiating water masers being 10^2 km s^{-1}, we obtain a lower limit for the disk size of $d_{\text{disk}} \approx 10^{15}$ cm. The lower limit is due to the fact that our monitoring did not begin with the onset of increased water maser activity. An important feature of Flare 0 is also that its velocity did not change over the entire observation period. This indirectly confirms our assumption that the source of this feature is an extended halo around the gas-dust disk.

Figure 21 shows the drift in the frequency of the maxima of Flares 1–9. The errors in the values of the flare frequency maxima were determined mainly by the accuracy of fitting the Gaussian curves to the radial spectral lines and amounted to about 0.01 km s^{-1} (one-third of the velocity resolution). The obtained dependence does not contradict the physical picture in which the source initiating the maser emission reaches successively maser concentrations located in a rotating gas-dust disk. The changes in the frequencies of the flare maxima occur sequentially, without sharp deviations. This can also be explained by the fact that the broad front of the shock waves propagates at a small angle to the line along which the water masers are located. Therefore, the partial overlap of maser spots with each other finds a natural explanation (see Fig. 17).

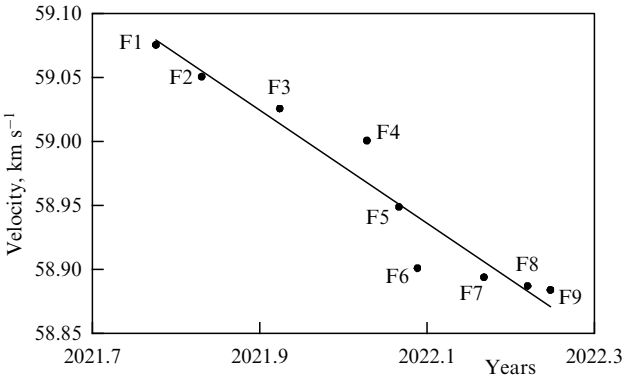

Figure 21. Drift of maxima frequencies of Flares 1–9.

It is known that around young massive stars in regions of active star formation there are gas and dust molecular disks with characteristic dimensions of about 10^{16} cm, in which maser spots (condensations) are located [114]. For example, according to interferometric maps, the radius of the molecular disk in W49N is $\sim 2 \times 10^{16}$ cm [115]. The same applies to W51 Main, which is a very dense cloud of gas and dust, including a massive ($30M_{\odot}$ or more) young O-class star with a rotating and simultaneously expanding disk of gas and dust with a diameter of $5 \times 10^{15} - 3 \times 10^{16}$ cm [116]. This physical picture of W51 Main may correspond to the structure and emission of a water maser near the singularity of the radial velocity 60 km s^{-1} that we discovered in our study of the giant flare phenomenon.

Our studies of W51 Main have established that, considering the duration of short powerful flares of 7 days at the half-flux density level, all 9 flares exist for about half a year [110]. With the propagation speed of shock waves initiating water masers of 10^2 km s^{-1} and the Flares 1–9 duration of 250 days each, we have linear dimensions of the maser cluster of about 10 au. Moreover, the volume of the maser cluster can accommodate a much greater number of condensations. In this case, we always assume that the source of the primary energy release is the partially ejected envelopes of binary supermassive stars rotating around a common center of gravity and experiencing powerful tidal gravitational interactions with each other.

If the masers are located in the outer parts of the gas-dust disk, we can determine a minimum disk size for features of about 60 km s^{-1}, assuming a central star mass of $30M_{\odot}$. We obtain a disk size of 3.4×10^{15} cm. This is 1.5 times smaller than the value obtained from interferometric observations for W51 Main by Genzel et al. [116]. This suggests that the central star mass may exceed $30M_{\odot}$.

3.5 Model of the primary energy release and estimate of the gravitational wave flux level

Giant flares of a water vapor maser must be provided by powerful sources of primary energy release, leading to an increase in the line flux density by hundreds of times. Such water vapor maser initiators include infrared emission from a molecular gas-dust cloud in which maser condensations are embedded, and/or a system of powerful shock waves propagating from a central stellar object. Bipolar ejections that excite maser sources may also serve as pumping sources. However, it remains unclear what exactly initiates the activity of central stellar objects, which may include both late-type

T-Taurus stars and massive early-type stars located near the main sequence.

There are a number of hypotheses regarding the mechanisms for initiating water vapor emission in galactic sources, which are associated with both changes in dust temperature and the photon flux density emanating from the central source.

Giant flares of water vapor masers in galactic kilomasers Orion KL, W49, W51, IRAS 18316-0602 occur rarely, no more than once every 5–10 years [102, 103, 110, 111]. What physical processes initiate these flares, during which the radiation flux densities in the lines can increase hundreds of times? There is no doubt that the main energy release in the system is provided by massive stars of early spectral classes, which are at the stage preceding the main sequence. The process of formation and evolution of such stars, as a rule, is hidden from our eyes due to giant absorption in the optical range in the direction of such stellar complexes. The emission spectra in the IR range have maxima in the far infrared region, which indicates noticeable absorption in this wavelength range. Only the radio range allows us to discern compact H II regions, indicating the presence of massive stars of early spectral types, ionizing the surrounding space out to distances of 10^{18} cm from the central, very massive star. However, the question remains as to whether a single star is ionizing the surrounding space, or several stars.

It is known that about half of the stars in galaxies are binary or multiple systems. They most likely formed during the evolution of a gas-dust cloud by fragmenting it into its component parts. A key aspect of this situation is the interaction of these multiple systems in terms of the possibility of initiating sources of primary energy release in gas-dust clouds. How do such sources lead to giant flares in kilomasers of water vapor?

Among the main mechanisms for excitation of H_2O masers, radiation and impact mechanisms are noted. The former is achieved through the transformation of quanta from the central star into an infrared source in the nebula, and the latter through a system of shock waves passing through the medium in which the maser globules are located. However, the question remains: what are the sources of giant energy release that explosively provide such powerful flares of water vapor masers?

Looking at the double flare of the H_2O maser in IRAS 18316-0602 and the flare event in W51 M, during which the maser was in an unsaturated state, one comes to the conclusion that this maser activation process took place over the course of a month, after which an exponential decline in the radiation flux density occurred [102, 110]. What process could have caused such pumping of H_2O molecules in an isolated maser globule? The presence of a narrow emission line at a fixed frequency indicates that the globule was unique. Such emission parameters in the line should be ensured by the globule's high density, its significant mass, and a large temperature difference persisting for a noticeable period of time, on the order of a month. Identifying a physical process that changes the characteristics of a maser globule, maintaining the maser unsaturated state for tens of days and ending as suddenly as it began, is apparently not so simple.

A powerful stellar wind most likely cannot be the source of such a primary energy release due to its low energy characteristics. Partial, multiple ejections of the star envelopes could, in principle, provide the energy for the process. Thus, with a velocity of the ejected envelope of $v \approx 5 \times 10^7$ cm s^{-1} (500 km s^{-1}), in a month it will move a distance of $l \approx 1.5 \times 10^{14}$ cm (10 au), which significantly exceeds the size of the maser globules. Consequently, for a maser globule to be in an activated state, the ejected envelope must have dimensions of approximately 10 au. The envelope ejection velocity may be even lower. Note that during supernova explosions, the velocity of matter movement can reach values of $v \approx 10^9$ cm s^{-1}. Thus, the considered mechanism of maser emission activation is quite probable.

The accretion mechanism is not very suitable because the latest flares of late 2016 and 2017–2018 in IRAS 18316-0602 are similar in duration, and it is simply illogical to imagine such regular accretion.

Models of hot, dense material in a rotating accretion disk [117] or pulsation-unstable massive stars [118] have also been proposed. In this case, the colliding stellar winds of binary stars [119] may be responsible for the proposed periodicity.

The source we observed does indeed exhibit a quasi-regular process, both in the duration of the flare and in the intervals between flares. The flares in IRAS 18316-0602 that occurred in 2002–2003, 2010, and at the end of 2016 — (2017–2018) do not exclude the presence of a quasi-period of explosive activity of approximately 7 years.

In addition, there is a possibility of the existence of binary flares. In addition to the binary flare in IRAS 18316-0602 (2017–2018), a binary flare was possibly observed in Orion KL in 1979–1980 [120], and a cascade of flares was observed in W51M [110].

These considerations lead to the idea that the source of such quasi-periodic activity may be compact multiple massive stellar systems. In particular, these may be triple stars. The quasiperiod is determined by the temporal stability of the system, in which the third body and the accretion disk itself violate the condition of harmonicity and, consequently, the stability of the flare period.

Let us estimate the orbital parameters of the system companions to achieve the observed characteristics of the water vapor maser flares in IRAS 18316-0602 [102, 103]. Using the laws of celestial mechanics, we can show that for a massive central star with a mass of $30M_\odot$ paired with a less massive object in an elliptical orbit with a semiaxis of 25 au, the orbital period around the common center of gravity will be approximately 8 years. This is precisely the quasiperiod observed between the water vapor maser hyperflares in the IRAS 18316-0602 system. At the periastron of the system, a powerful gravitational perturbation of the very massive central star occurs, leading to a partial ejection of its envelope.

The ejected envelope, reaching the accretion disk where the maser globules are located, creates a powerful shock wave system, leading to an explosive increase in the temperature and density of the maser globule. This leads to an exponential increase in maser pumping during the entire passage of the envelope. After the end of maser activation, an exponential decrease in the radiation flux density occurs due to a decrease in the H_2O vapor density and the temperature and density of the maser globule material.

The question of the possibility of gravitational wave (GW) emission from close binary star systems (CBSs) has been posed for the first time and is based on new experimental data and detailed information obtained regarding maser emission arising in dense, massive gas-dust complexes [110, 121].

One of effective mechanisms for increasing the density of the medium is the influence of stellar wind. In this case, the H_2O maser sources are sites of interaction between the stellar wind of the forming star and gas clumps in its envelope. In any

case, the primary source of energy release in the system is a close massive binary star whose components are moving in elliptical orbits around a common center of gravity. During the periastron of the system, increasing gravitational-tidal interactions between the stars can lead to the ejection of portions of their envelopes into space. This can lead to a powerful stellar wind, leading to flares of water masers located in the gas and dust disk around the binary system.

The central star ($\approx 30M_{\odot}$) may have a companion with a mass equal to tens of solar masses. During gravitational-tidal interactions with each other during the periastron of the system, the envelopes of one or the other star can be ejected into the surrounding space [122]. A supersonic shock wave propagates through a gas-dust disk containing maser condensations. In this case, massive CBSs may be responsible for giant water maser flares in galactic kilomasers such as W49N and W51 Main.

If CBSs are located in a zone of active star formation, the strength of gravitational waves emanating from them can be estimated by assuming that they are in a phase close to merging. These systems can emit gravitational waves [123]. The GW power from these objects and the flux density S_{Earth} at the Earth's surface are

$$\frac{\mathrm{d}E}{\mathrm{d}t}=L=\left\{\frac{32G^4m_1^2m_2^2(m_1+m_2)(1+3.5e^2+1.4e^4)}{5c^5a^5(1-e^2)^{1/2}}\right\}\ \mathrm{erg\ s^{-1}}, \tag{20}$$

$$S_{\mathrm{Earth}}=\frac{L}{4\pi}\,R^2\,. \tag{21}$$

Here, L is the luminosity (radiation power), S_{Earth} is the flux density at the Earth's surface, m_1 is the mass of the central star, m_2 is the mass of the satellite, e is the eccentricity, a is the major semiaxis of the orbit, c is the speed of light, and R is the distance from the source to the Earth.

To obtain specific numerical values, we can take $R_{\mathrm{W51}} =$ 5 kpk, $m_1 = m_2 = 30M_{\odot}$, $e = 0.7$, $a = 5 \times 10^{11}$ cm. Then we have $\mathrm{d}E/\mathrm{d}t_{\mathrm{W51}} \approx 2.2 \times 10^{36}$ erg s^{-1}. This gives the flux density at the Earth's surface $S_{\mathrm{W51,\,Earth}} \approx 0.9 \times 10^{-9}$ erg cm^{-2} s^{-1}. This is quite comparable with the calculated value of the GW flux density at the Earth's surface from such a well-known source as OJ 287. It is necessary to consider the difference in distances between W51 Main and OJ 287: $R_{\mathrm{OJ287}} \approx 3.3 \times 10^{27}$ cm, $m_1 \approx 10^{10}M_{\odot}$, $m_2 \approx 10^{8}M_{\odot}$, $e \approx 0.7$, $a \approx 10^4$ au. We obtain a value for the GW flux density from OJ 287 at the Earth's surface of $S \approx 0.7 \times 10^{-9}$ erg cm^{-2} s^{-1} [124].

Consequently, to have comparable flux densities near the Earth from W51 Main and OJ 287, the companions in W51 must be very close to each other and separated by about ten stellar radii. Such binary massive stellar systems are indeed at a stage of evolution close to their merger. The energy loss for the G 25.65 + 1.05 kilomaser due to GW emission will be $\approx 2.3 \times 10^{34}$ erg^{-1}, and thus, on the Earth's surface, the GW flux density from the object will be $\approx 0.5 \times 10^{-11}$ erg cm^{-2} s^{-1} [121]. This is two orders of magnitude lower than the GW level from the brightest AGN [124–129]. However, there are regions of active star formation in the Galaxy closer to the Earth than W51 Main, for example, W3 and many others [130–132]. Therefore, the detection of GW from CBSs is an urgent task.

An important conclusion was obtained that galactic massive CBSs, along with supermassive black holes such as OJ 287, are promising for detecting gravitational waves from them in the range of $\approx 10^{-6}$–10^{-7} Hz using IPTA (International Pulsar Timing Array) — a gravitational wave detector operating at this low frequency and possessing the high sensitivity necessary to register such low flux densities [133]. This opens new broad potential for further research of gravitational waves with the aim of their experimental detection.

3.6 Conclusions

(1) Using the RT-22 radio telescope, the phenomenon of giant maser flares of water vapor in galactic sources was discovered. Two kilomasers were detected: IRAS 18316-0602 and W51 Main, one of which, IRAS 18316-0602, is recognized as the most powerful in the Galaxy. This discovery was included in the annual report of the Russian Academy of Sciences to the President of the Russian Federation as one of the most significant results in astrophysics for 2019. Such results were obtained for the first time in the world.

(2) Long-term monitoring of the galactic kilomasers IRAS 18316-0602 (G 25.65 + 1.05) and W51 M in the water vapor line ($6_{16}-5_{23}$ transition, line frequency $f =$ 22.235 GHz) was carried out using the RT-22 radio telescope of the Crimean Astrophysical Observatory. The unique double flare of 2017–2018 in the IRAS 18316-0602 source demonstrated an exponential increase in the radiation flux density, which indicates an unsaturated state of the masers during the entire flare. This is also confirmed by the relatively low degree of linear polarization ($\sim 30\%$).

(3) In the source W51 Main, a flare phenomenon unprecedented in amplitude and duration was observed, caused by the superposition of several powerful short Flares 1–9 on a longer, but less powerful Flare 0. The latter had a broad spectral line, characteristic of a saturated maser, while the short flares were caused by unsaturated masers with narrow lines. New important physical parameters of the flares of the water maser W51 Main were obtained: the states of the water maser during the flares, their amplitudes, the widths of the maser lines, the kinetic temperatures of H_2O, and the presence of cascade amplification of the water maser, necessary for the occurrence of high-power short flares.

(4) Observational data have established that the most powerful water masers are created by the combined emission of several unsaturated maser spots along the observer's line of sight, each of which successively amplifies the maser emission, transferring it to the next maser condensation, resulting in ultra-high-power emission. Powerful short flares are located above less powerful but longer-lasting ones. The broad Doppler spectral lines of less powerful flares indicate that their masers are likely in a saturated state, while the masers of more powerful flares with narrow lines are in an unsaturated state. The resulting pattern of cascade amplification is new and fundamental for explaining the physical nature of maser amplification and emission.

(5) It was found that the generation of high-power water masers requires input flux densities exceeding several kJy, which may indicate a high density of maser spots (up to hundreds of units) in compact clusters.

(6) A model for the energy release is proposed according to which maser flares are associated with gravitational perturbations in close binary star systems, especially during their merger phase. In this context, powerful maser flares can be considered as potential electromagnetic indicators of gravitational wave generation in the vicinity of massive binary systems.

Acknowledgments. This study used data from the 40-m OVRO radio telescope monitoring program, which is funded in parts by NASA (grants NNX08AW31G, NNX11A043G, NNX14AQ89G) and NSF (grants AST-0808050 and AST-1109911). Optical data were used from the Steward Observatory project of spectropolarimetric monitoring, supported by NASA through the Fermi Guest Investigator program (grants NNX08AW56G, NNX09AU10G, NNX12AO93G, and NNX15AU81G) and from the Stefan Karge quasar monitoring project (Steward Karge, Frankfurt).

References

1. Sillanpaa A et al. *Astron. Astrophys.* **305** L17 (1996)
2. Volvach A E et al. *Astron. Rep.* **51** 450 (2007); *Astron. Zh.* **84** 503 (2007)
3. Volvach A, Volvach L, Larionov M *Galaxies* **11** (5) 96 (2023)
4. Volvach A E, Volvach L N, Larionov M G *Astron. Astrophys.* **648** A27 (2021)
5. Volvach A E, Volvach L N, Larionov M G *Astron. Astrophys.* **691** L9 (2024)
6. Volvach A et al. *Bull. Lebedev Phys. Inst.* **51** 100 (2024); *Kratk. Soobshch. Fiz. FIAN* (4) 100 (2024)
7. Richards J L et al. *Astrophys. J. Suppl.* **194** 29 (2011)
8. Wen L et al. *Astrophys. J. Suppl.* **163** 372 (2006) DOI:10.1086/500648
9. Claudi R et al. *Commun. Asteroseismol.* **145** 53 (2004) DOI:10.1553/cia145s51
10. Lanza A F, Rodono M, Zappala R A *Astron. Astrophys.* **269** 351 (1993)
11. Barning F J M *Bull. Astron. Inst. Netherlands* **17** 22 (1963)
12. Lomb N R *Astrophys. Space Sci.* **39** 447 (1976)
13. Scargle J D *Astrophys. J.* **263** 835 (1982)
14. Deeming T *Astrophys. Space Sci.* **36** 137 (1975)
15. Vityazev V V *Analiz Neravnomernykh Vremennykh Ryadov* (Analysis of Unevenly Spaced Time Series) (St. Petersburg: Izd. St. Petersburg. Univ., 2001)
16. Roberts D H, Lehar J, Dreher J W *Astron. J.* **93** 968 (1987)
17. Horne J H, Baliunas S L *Astrophys. J.* **302** 757 (1986)
18. Roy A et al. *Mon. Not. R. Astron. Soc.* **513** 5238 (2022)
19. Edelson R A, Krolik J H *Astrophys. J.* **333** 646 (1988)
20. Birks J B *The Theory and Practice of Scintillation Counting* (Oxford: Pergamon Press, 1964) DOI:10.1016/C2013-0-01791-4
21. Fujisawa K et al. *Publ. Astron. Soc. Jpn.* **51** 537 (1999)
22. Padovani P et al. *Mon. Not. R. Astron. Soc.* **347** 1282 (2004)
23. Escudero Pedrosa J et al. *Astron. Astrophys.* **682** A100 (2024)
24. Vol'vach A E et al. *Astron. Rep.* **59** 145 (2015); *Astron. Zh.* **92** 168 (2015)
25. Caproni A, Abraham Z *Mon. Not. R. Astron. Soc.* **349** 1218 (2004)
26. Aller M F et al., in *Variability of Blazars. Proc. of the Conf. in Honour of the 100th Anniversary of the Birth of Yrjö Väisälä* (Eds E Valtaoja, M Valtonen) (Cambridge: Cambridge Univ. Press, 1992) p. 126
27. Sillanpaa A et al. *Astrophys. J.* **325** 628 (1988)
28. Shukla H, Stoner R E *Astrophys. J. Suppl.* **106** 41 (1996)
29. Pietilä H et al. *Astron. Astrophys.* **345** 760 (1999)
30. Massaro E et al. *Astron. Astrophys.* **495** 691 (2009)
31. Roy A et al. *Mon. Not. R. Astron. Soc.* **513** 5238 (2022)
32. Dunn R J H, Fabianos A C, Sanders J S *Mon. Not. R. Astron. Soc.* **366** 758 (2006)
33. Suleimanov V F, Lipunova G V, Shakura N I *Astron. Rep.* **51** 549 (2007); *Astron. Zh.* **84** 612 (2007)
34. McClintock J E et al. *Astrophys. J.* **258** 245 (1982)
35. Ioannou Z et al. *Astron. Astrophys.* **382** 130 (2002)
36. Vol'vach A E et al. *Astron. Rep.* **53** 777 (2009); *Astron. Zh.* **86** 835 (2009)
37. Valtonen M J et al. *Nature* **452** 851 (2008)
38. Dey L et al. *Astrophys. J.* **866** 11 (2018)
39. Graham M J et al. *Nature* **518** 74 (2015)
40. Caproni A, Abraham Z *Proc. Int. Astron. Union* **2004** (IAU222) 83 (2004) DOI:10.1017/S1743921304001541
41. Lister M L et al. *Astron. J.* **137** 3718 (2009)
42. Shen Y et al. *Astrophys. J.* **775** 49 (2013)
43. Eracleous M et al. *Astrophys. J. Suppl.* **201** 23 (2012)
44. Tsalmantza P et al. *Astrophys. J.* **738** 20 (2011)
45. Rodriguez C et al. *Astrophys. J.* **646** 49 (2006)
46. Bansal K et al. *Astrophys. J.* **843** 14 (2017)
47. Boccardi B et al. *Astron. Astrophys. Rev.* **25** 4 (2017)
48. Lobanov A P, Roland J *Astron. Astrophys.* **431** 831 (2005)
49. Britzen S et al. *Mon. Not. R. Astron. Soc.* **478** 3199 (2018)
50. D'Orazio D J et al. *Mon. Not. R. Astron. Soc.* **436** 2997 (2013)
51. Farris B D et al. *Mon. Not. R. Astron. Soc.* **447** 80 (2015)
52. Noble S C et al. *Astrophys. J.* **755** 51 (2012)
53. Sergeev S G, Nazarov S V, Borman G A *Mon. Not. R. Astron. Soc.* **465** 1898 (2017)
54. Charisi et al. *Mon. Not. R. Astron. Soc.* **463** 2145 (2016)
55. Liu X et al. *Astrophys. J. Lett.* **803** L16 (2015)
56. Graham M J et al. *Nature* **518** 74 (2015)
57. Burke-Spolaor S et al. *Astron. Astrophys. Rev.* **27** 5 (2019)
58. Antoniadis J et al. *Mon. Not. R. Astron. Soc.* **510** 4873 (2022)
59. Fernandez J J, Kobayashi S *Mon. Not. R. Astron. Soc.* **487** 1200 (2019)
60. Regimbau T et al. *Astrophys. J.* **799** 69 (2015)
61. Mingarelli C M F et al. *Nature Astron.* **9** 183 (2025)
62. Peters P C *Phys. Rev.* **136** B1224 (1964)
63. Sun Y-T et al. *Chinese Astron. Astrophys.* **35** 123 (2011)
64. Valtonen M J et al. *Nature* **452** 851 (2008)
65. Fang Y, Yang H *Mon. Not. R. Astron. Soc.* **523** 5120 (2023)
66. Manchester R N *Chinese J. Astron. Astrophys.* **6** 139 (2006)
67. Fish V L, Shea M, Akiyama K *Adv. Space Res.* **65** 821 (2020)
68. Zel'dovich Ya B, Novikov I D *Stroenie i Evolyutsiya Vselennoi* (The Structure and Evolution of the Universe) (Moscow: Nauka, 1975)
69. Bochkarev N G *Osnovy Fiziki Mezhzvezdnoi Sredy* (Fundamentals of the Physics of the Interstellar Medium) 2nd ed. (Moscow: URSS 2010)
70. Tielens A G G M *The Physics and Chemistry of the Interstellar Medium* (Cambridge: Cambridge Univ. Press, 2005)
71. Elitzur M *Astronomical Masers* (Astrophysics and Space Science Library, Vol. 170) (Dordrecht: Kluwer Acad., 1992) DOI:10.1007/978-94-011-2394-5
72. Douglas A E, Herzberg G *Astrophys. J.* **94** 381 (1941)
73. Weinreb S et al. *Nature* **200** 829 (1963)
74. Wootten A, Thompson A R *Proc. IEEE* **97** 1463 (2009)
75. McGuire B A *Astrophys. J. Suppl.* **259** 30 (2022)
76. Krumholz M R *Phys. Rep.* **539** 49 (2014)
77. Federrath C, Klessen R S *Astrophys. J.* **761** 156 (2012)
78. Burke B F et al. *Sov. Astron.* **16** 379 (1972); *Astron. Zh.* **49** 465 (1972)
79. Johnston K J et al. *Astrophys. J.* **166** L21 (1971)
80. Letokhov V, Johansson S *Astrophysical Lasers* (Oxford: Oxford Univ. Press, 2008) DOI:10.1093/acprof:oso/9780199548279.001.0001
81. Gray M *Maser Sources in Astrophysics* (Cambridge: Cambridge Univ. Press, 2012) DOI:10.1017/CBO9780511977534
82. Reid M J, Moran J M *Annu. Rev. Astron. Astrophys.* **19** 231 (1981) DOI:10.1146/annurev.aa.19.090181.001311
83. Volvach A E, Volvach L N, Larionov M G *Astrophys. J.* **955** 10 (2023)
84. Migenes V, Reid M J (Eds) *Cosmic Masers: From Proto-Stars to Black Holes, IAU Symp. 206, 5–10 March 2001, Rio de Janeiro, Brazil* (ASP Conf. Ser., Vol. 206) (San Francisco, CA: Astronomical Society of the Pacific, 2002)
85. Elitzur M *Annu. Rev. Astron. Astrophys.* **30** 75 (1992) DOI: 10.1146/annurev.aa.30.090192.000451
86. Volvach L N, Volvach A E, Strepka I D *Astron. Astrophys. Trans.* **25** 379 (2006)
87. Volvach A E *Infokommunikatsion. Radioelektron. Tekhnol.* **2** (1) 13 (2019)
88. Volvach A E, Volvach L N, Larionov M G *Mon. Not. R. Astron. Soc. Lett.* **496** L147 (2020)
89. Volvach A E et al. *Mon. Not. R. Astron. Soc. Lett.* **494** L59 (2020)
90. Volvach L N et al. *Mon. Not. R. Astron. Soc. Lett.* **487** L77 (2019)
91. Volvach L N et al. *Astron. Astrophys.* **628** A89 (2019)
92. Palla F et al. *Astron. Astrophys.* **246** 249 (1991)
93. Lekht E E et al. *Astron. Rep.* **62** 213 (2018); *Astron. Zh.* **95** 224 (2018)
94. Volvach A E et al., The Astronomer's Telegram, No. 10728 (2017)
95. Volvach A E et al., The Astronomer's Telegram, No. 10853 (2017)

96. Goldreich P, Keeley D A, Kwan J Y *Astrophys. J.* **179** 111 (1973)
97. Omodaka T et al. *Publ. Astron. Soc. Jpn.* **51** 333 (1999)
98. Shimoikura T et al. *Astrophys. J.* **634** 459 (2005)
99. Abraham Z et al. *Astron. Astrophys.* **100** L10 (1981)
100. Abraham Z, Vilas Boas J W S, del Ciampo L F *Astron. Astrophys.* **167** 311 (1986)
101. Goldreich P, Kwan J *Astrophys. J.* **190** 27 (1974)
102. Volvach L N et al. *Mon. Not. R. Astron. Soc. Lett.* **482** L90 (2019)
103. Vol'vach L N et al. *Astron. Rep.* **63** 49 (2019); *Astron. Zh.* **96** 51 (2019)
104. Westerhout G *Bull. Astron. Inst. Netherlands* **14** 215 (1958)
105. Ginsburg A et al. *Astrophys. J.* **842** 92 (2017)
106. Goldader J D, Wynn-Williams C G *Astrophys. J.* **433** 164 (1994)
107. Figueredo E et al. *Astron. J.* **136** 221 (2008)
108. Kang M et al. *Astrophys. J.* **706** 83 (2009)
109. Sato M et al. *Astrophys. J.* **720** 1055 (2010)
110. Volvach A E, Volvach L N, Larionov M G *Astrophys. J.* **955** 10 (2023)
111. Volvach A E, Volvach L N, Larionov M G *Astron. J.* **64** 66 (2022)
112. Goldreich P, Kwan J *Astrophys. J.* **190** 27 (1974)
113. Volvach L N, Volvach A E, Larionov M G *Infokommunikatsion. Radioelektron. Tekhnol.* **5** (2) 153 (2022)
114. White G J *Mon. Not. R. Astron. Soc.* **186** 377 (1979)
115. Walker R C et al. *Astrophys. J.* **211** L135 (1977)
116. Genzel R et al. *Astron. Astrophys.* **78** 239 (1979)
117. Hirota T et al. *Astrophys. J. Lett.* **739** L59 (2011)
118. Parfenov S, Sobolev Yu *Mon. Not. R. Astron. Soc.* **444** 620 (2014)
119. Hollenbach D, Elitzur M, McKee C F *Astrophys. J.* **773** 70 (2013)
120. Maswanganye J P et al. *Mon. Not. R. Astron. Soc.* **446** 2730 (2015)
121. Volvach A E, Volvach L N, Larionov M G *J. Astrophys. Astron.* **45** 32 (2024)
122. Volvach L N et al. *Astron. Rep.* **63** 652 (2019); *Astron. Zh.* **96** 638 (2019)
123. Manchester R N *Chinese J. Astron. Astrophys. Suppl.* **6** 139 (2006)
124. Volvach A E, Volvach L N, Larionov M G *iScience* **27** (4) 109427 (2024) DOI:10.1016/j.isci.2024.109427
125. Volvach A E, Volvach L N, Larionov M G *Astron. Astrophys.* **648** A27 (2021)
126. Volvach A, Volvach L, Larionov M *Astrophys. J.* **992** 60 (2025) DOI:10.3847/1538-4357/adfee2
127. Volvach A E, Volvach L N, Larionov M G *Astron. Astrophys.* **691** L9 (2024)
128. Burns R A et al. *Nature Astron.* **7** 557 (2023) DOI:10.1038/s41550-023-01899-w
129. Volvach A E et al. *Cosmic Res.* **57** 85 (2019); *Kosmich. Issled.* **57** (2) 99 (2019)
130. Volvach A E, Volvach L N, Larionov M G *Mon. Not. R. Astron. Soc. Lett.* **522** L6 (2023)
131. Volvach A E, Volvach L N, Larionov M G *Mon. Not. R. Astron. Soc.* **507** L52 (2021)
132. Volvach A E, Volvach L N, Larionov M G *Astron. Astrophys.* **672** A182 (2023)
133. Manchester R N *Class. Quantum Grav.* **30** 224010 (2013) DOI:10.1088/0264-9381/30/22/224010